

# AD-A259 829



## MENTATION PAGE

Form Approved  
OMB No. 0704-0188



It is estimated to average 1 hour per response, including the time for reviewing instructions, searching existing data sources, gathering and reviewing the collection of information. Send comments regarding this burden estimate or any other aspect of this collection of information, including this burden, to Washington Headquarters Services, Directorate for Information Operations and Reports, 1215 Jefferson Avenue, Washington, DC 20540, and to the Office of Management and Budget, Paperwork Reduction Project (0704-0188), Washington, DC 20503.

1. REPORT DATE 1-26-93		3. REPORT TYPE AND DATES COVERED Annual 10/1/91 - 9/30/92	
4. TITLE AND SUBTITLE Three Dimensional Transient Analysis of Microstrip Circuits in Multilayered Anisotropic Media		5. FUNDING NUMBERS N00014-90-J-1002	
6. AUTHOR(S) Prof. J.A. Kong		4143124-05	
7. PERFORMING ORGANIZATION NAME(S) AND ADDRESS(ES) Research Laboratory of Electronics Massachusetts Institute of Technology 77 Massachusetts Avenue Cambridge, MA 02139		8. PERFORMING ORGANIZATION REPORT NUMBER	
9. SPONSORING/MONITORING AGENCY NAME(S) AND ADDRESS(ES) Office of Naval Research 800 North Quincy St. Arlington, VA 22217		10. SPONSORING/MONITORING AGENCY REPORT NUMBER	
11. SUPPLEMENTARY NOTES The view, opinions and/or findings contained in this report are those of the author(s) and should not be construed as an official Department of the Army position, policy, or decision, unless so designated by other documentation.			
12a. DISTRIBUTION/AVAILABILITY STATEMENT Approved for public release; distribution unlimited.		12b. DISTRIBUTION CODE	
13. ABSTRACT (Maximum 200 words)  Work by Prof. Kong and his collaborators is summarized here			
14. SUBJECT TERMS		15. NUMBER OF PAGES	
		16. PRICE CODE	
17. SECURITY CLASSIFICATION OF REPORT UNCLASSIFIED		18. SECURITY CLASSIFICATION OF THIS PAGE UNCLASSIFIED	19. SECURITY CLASSIFICATION OF ABSTRACT UNCLASSIFIED
			20. LIMITATION OF ABSTRACT UL

**DTIC**  
**ELECTE**  
**FEB 02 1993**  
**S B**

304050

**93-01795**



**ANNUAL REPORT**

**Title: THREE DIMENSIONAL TRANSIENT ANALYSIS OF MICROSTRIP CIRCUITS IN  
MULTILAYERED ANISOTROPIC MEDIA**

**Sponsor by: Department of the Navy/Office of Naval Research**

**Contract number: N00014-90-J-1002**

**Research Organization: Center for Electromagnetic Theory and Applications  
Research Laboratory of Electronics  
Massachusetts Institute of Technology**

**OSP number: 72943**

**Principal Investigator: J. A. Kong**

**Period covered: October 1, 1991 — September 30, 1992**

## Three Dimensional Transient Analysis of Microstrip Circuits in Multilayered Anisotropic Media

Under the sponsorship of the ONR contract N00014-90-J-1002 we have published 12 refereed journal and conference papers.

The finite difference-time domain (FD-TD) technique is applied to the solution of Maxwell's equations. A computer program, which can be used to simulate and study numerous electromagnetic phenomena, is developed and implemented on an IBM 386 compatible personal computer. The FD-TD technique is a useful tool for students in electromagnetics. The technique is flexible and can be applied to many basic EM scattering and radiation problems. Because field solutions are found as a function of time, visualization of the propagation of the EM fields is possible. The FD-TD technique is implemented for a two-dimensional rectangular grid in conjunction with a second-order absorbing boundary condition. Both E- and H-field polarizations are analyzed. Finite objects consisting of dielectric, magnetic and conducting materials, and perfectly conducting infinite ground planes are modeled. Plane wave and line current sources are implemented. In addition to the capability of animating the propagation of the EM fields, radiation and scattering patterns can be generated.

A methodology developed to handle dispersive materials in the time domain is extended to model the dispersive characteristics of the impedance boundary condition used for a thin layer coating over perfect conductors. The impedance boundary condition is first approximated as a rational function of frequency. This rational function is then transformed to a time domain equation, resulting in a partial differential equation in space and time. Discretization of the time domain model to efficiently handle the thin layer coating is presented in the context of the finite-difference time-domain (FD-TD)

technique. The methodology is verified by solving a one-dimensional problem using the FD-TD technique and comparing with the analytical results.

To understand the physical meaning of rational reflection coefficients in inverse-scattering theory for optical waveguide design, we studied the relationship between the poles of the transverse reflection coefficient and the modes in inhomogeneous dielectrics. By using a stratified-medium formulation we showed that these poles of the spectral reflection coefficient satisfy the same equation as the guidance condition in inhomogeneous waveguides. Therefore, in terms of wave numbers, the poles are the same as the discrete modes in the waveguide. The radiation modes have continuous real values of transverse wave numbers and are represented by the branch cut on the complex plane. Based on these results, applications of the Gel'fand-Levitan-Marchenko theory to optical waveguide synthesis with the rational function representation of the transverse reflection coefficient are discussed.

The coupled-wave theory is generalized to analyze the diffraction of waves by chiral gratings for arbitrary angles of incidence and polarizations. Numerical results for the Stokes parameters of diffracted Floquet modes versus the thickness of chiral gratings with various chiralities are calculated. Both horizontal and vertical incidences are considered for illustration. The diffracted waves from chiral gratings are in general elliptically polarized; and in some particular instances, it is possible for chiral gratings to convert a linearly polarized incident field into two nearly circularly polarized Floquet modes propagating in different directions.

A general spectral domain formulation to the problem of radiation of arbitrary distribution of sources embedded in a horizontally stratified arbitrary magnetized linear plasma is developed. The fields are obtained in terms of electric and magnetic type dyadic Green's functions. The formulation is considerably simplified by using the kDB system of coordinates in conjunction with the Fourier transform. The distributional singular

behavior of the various dyadic Green's functions in the source region is investigated and taken into account by extracting the delta function singularities. Finally, the fields in any arbitrary layer are obtained in terms of appropriately defined global upward and downward reflection and transmission matrices.

We investigated a method for the calculation of the current distribution, resistance, and inductance matrices for a system of coupled superconducting transmission lines having finite rectangular cross section. These calculations allow accurate characterization of both high- $T_c$  and low- $T_c$  superconducting strip transmission lines. For a single stripline geometry with finite ground planes, the current distribution, resistance, inductance, and kinetic inductance are calculated as a function of the penetration depth for various film thickness. These calculations are then used to determine the penetration depth for  $Nb$ ,  $NbN$ , and  $YBa_2Cu_3O_{7-x}$  superconducting thin films from the measured temperature dependence of the resonant frequency of a stripline resonator. The calculations are also used to convert measured temperature dependence of the quality factor to the intrinsic surface resistance as a function of temperature for a  $Nb$  stripline resonator.

The electromagnetic radiation from a VLSI chip package and heatsink structure is analysed by means of the finite-difference time-domain (FD-TD) method. The FD-TD algorithm implemented incorporates a multi-zone gridding scheme to accommodate fine grid cells in the vicinity of the heatsink and package cavity and sparse gridding in the remainder of the computational domain. The issues pertaining to the effects of the heatsink in influencing the overall radiating capacity of the configuration are addressed. Analyses are facilitated by using simplified heatsink models and by using dipole elements as sources of electromagnetic energy to model the VLSI chip. The potential for enhancement of spurious emissions by the heatsink structure is examined. For heatsinks of typical dimensions, resonance is possible within the low gigahertz frequency range.

Because the effects of diffraction during proximity-print x-ray lithography are of

DTIC QUALITY INSPECTED 3

Dist	Special
A-1	

<input checked="" type="checkbox"/>
<input type="checkbox"/>
<input type="checkbox"/>
Code
1/82

critical importance, a number of previous researchers have attempted to calculate the diffraction patterns and minimum achievable feature sizes as a function of wavelength and gap. Work to date has assumed that scalar diffraction theory is applicable—as calculated, for example, by the Rayleigh-Sommerfeld formulation—and that Kirchhoff boundary conditions can be applied. Kirchhoff boundary conditions assume that the fields (amplitude and phase) are constant in the open regions between absorbers, and a different constant in regions just under the absorbers (i.e., that there are no fringing fields). An x-ray absorber is, however, best described as a lossy dielectric that is tens or hundreds of wavelengths tall, and hence Kirchhoff boundary conditions are unsuitable. We have instead used two numerical techniques to calculate accurate diffracted fields from gold absorbers for two cases: a 30 nm-wide line at  $\lambda = 4.5$  nm, and a 100 nm-wide line at  $\lambda = 1.3$  nm. We show that the use of Kirchhoff boundary conditions introduces unphysically high spatial frequencies into the diffracted fields. The suppression of these frequencies—which occurs naturally without the need to introduce an extended source or broad spectrum—improves exposure latitude for mask features near  $0.1 \mu\text{m}$  and below.

In order to understand the physical meaning of rational reflection coefficients in one-dimensional inverse scattering theory for optical waveguide design, we have studied the relation between the poles of the transverse reflection coefficient and the modes in inhomogeneous dielectrics. By using a stratified medium model it is shown that these poles of the reflection coefficient have a one-to-one correspondence to the discrete modes, which are the guided and leaky modes. The radiation modes have continuous real values of transverse wave numbers and are not represented by the poles of the reflection coefficient. Based on these results, applications of the Gel'fand-Levitan-Marchenko theory to optical waveguide synthesis with the rational function representation of the transverse reflection coefficient are investigated.

In compact modules of high performance computers, signal transmission lines be-

tween integrated circuit chips are embedded in multilayered dielectric medium. These signal lines are usually placed in different layers and run perpendicular to each other. The interaction between the orthogonal crossing lines and the signal line affects its propagation characteristics and may cause considerable signal distortion.

The interaction of a pair of crossing lines in isotropic medium has been studied using a time-domain approach, where coupling is described qualitatively. This method becomes computationally expensive when the number of crossing lines increases. With many identical crossing strips uniformly distributed above the signal line, the transmission properties are characterized by stopbands due to the periodicity of the structure. Periodic structure have been investigated using frequency-domain methods. Periodically nonuniform microstrip lines in an enclosure are analyzed on the basis of a numerical field calculation. A technique based on the network-analytical formulism of electromagnetic fields has been used to analyze striplines and finlines with periodic stubs. The propagation characteristics of waves along a periodic array of parallel signal lines in a multilayered isotropic structure in the presence of a periodically perforated ground plane and that in a mesh-plane environment have been studied. More recently, the effect of the geometrical properties on the propagation characteristics of strip lines with periodic crossing strips embedded in a shielded one-layer isotropic medium have been investigated. Both open and closed multilayered uniaxially anisotropic structures are considered. A full-wave analysis is used to study the propagation characteristics of a microstrip line in the presence of crossing strips. The signal line and the crossing strips are assumed to be located in two arbitrary layers of a stratified uniaxially anisotropic medium. An integral equation formulation using dyadic Green's functions in the periodically loaded structure is derived. Galerkin's method is then used to obtain the eigenvalue equation for the propagation constant. The effects of anisotropy on the stopband properties are investigated. Numerical results for open and shielded three-layer uniaxially anisotropic media are presented.

For microwave integrated circuit applications, the characteristics of interconnects have been investigated for the propagation modes, time response, crosstalk, coupling, delay, etc. In these analyses, it is assumed that quasi-TEM modes are guided along the multiconductor transmission lines. The analysis were performed for arbitrary number of transmission lines where the load and the source conditions were presented in terms of the modal reflection and transmission coefficient matrices.

To perform the quasi-TEM analysis, the capacitance matrix for the multiconductor transmission line has to be obtained first. Both the spectral and the spatial domain methods have been proposed to calculate the capacitance matrix. In the spectral domain methods, two side walls are used to enclose the whole transmission line structure, and the thickness of the strip lines has not been considered. In using the spatial domain method, the structure has to be truncated to a finite extent to make the numerical implementation feasible. The infinite extent of the structure was also incorporated, but only a two-layer medium was considered.

In practical microwave integrated circuits, the dielectric loss due to the substrate and the conductor loss due to the metallic strips are also studied in the analysis of circuit performances.

Based on the scalar Green's function, a set of coupled integral equations is obtained for the charge distribution on the strip surfaces. Pulse basis functions and a point-matching scheme is used to solve numerically the set of integral equations for the charge distribution, and hence the capacitance matrix. The duality between the electrostatic formulation and the magnetostatic one is applied to calculate the inductance matrix. The conductance matrix is obtained by using the duality between the electrostatic problem and the current field problem. A perturbation method is used to calculate the resistance matrix.

Finally, a transmission line analysis is derived to obtain the transfer matrix for multi-conductor uniform lines, which significantly reduces the effort in treating the load and the source conditions. Transient responses are obtained by using the Fourier transform. The results for two coupled lines are obtained.

With the ever increasing speed and density of modern integrated circuits, the need for electromagnetic wave analysis of phenomena such as the propagation of transient signals, especially the distortion of signal pulses, becomes crucial. One of the most important causes of pulse distortion is the frequency dependence of conductor loss, which is caused by the "skin effect", and which can be incorporated into the circuit models for transmission lines as frequency-dependent resistance and inductance per unit length. Efficient and accurate algorithms for calculating these parameters are increasingly important.

We have developed a hybrid cross-section finite element/coupled integral equation method. The technique is a combination of a cross-section finite element method, which is best for high frequencies. An interpolation between the results of these two methods gives very good results over the entire frequency range, even when few basis functions are used.

In the cross-section method, we divide each conductor into triangular patches and choose one of the patches from the return conductor to be our reference. We then calculate the resistance and inductance matrices for the patches. Using two conditions on the system, that the total current in each wire is the sum of the currents in the patches, and that the voltage on each patch in a wire must be the same (no transverse currents), we can reduce the matrices for the patches to the matrices for the wires. In the Weeks method, the patches are rectangles, and the quadruple integral is done quite easily in closed form. However, it is also possible to evaluate the quadruple integral in closed form for triangular patches, although the mathematics leading to this result is quite involved, and the final form of the answer is complicated. We therefore use triangular patches as the most flexible means of modelling conductors with arbitrary cross-sections; polygons are covered exactly,

and we are able to model quite closely other shapes, such as circles.

As frequency increases, the need to keep the uniform current approximation valid in the patches requires either the addition of many more patches as the skin depth decreases, or a redistribution of the existing patches to the surface, where the current is. However, changing the distribution of patches makes it necessary to recalculate the resistance and inductance matrices of the patches, thus increasing the computation time. Since we use a surface integral equation method for high frequencies, we do not change the distribution of the triangular patches for the cross-section method as we increase the frequency.

For high frequencies, we use a coupled surface integral equation technique. Under the quasi-TEM assumption, the frequency-dependent resistance and inductance result from the power dissipation and magnetic stored energy, which can be calculated by solving a magnetoquasistatic problem, with the vector potential satisfying Laplace's equation in the region outside all the conductors. The resistance and inductance are usually given by integrals of these field quantities over the cross-sections of the wires, but by using some vector identities it is possible to convert these expressions to integrals only over the surfaces of the wires. These expressions contain only the current at the surface of each conductor, the derivative of that current normal to the surface, and constants of the vector potential. A coupled integral equation is then derived to relate these quantities through Laplace's equation and its Green's function outside the conductors and the diffusion equation and its Green's function inside the conductors. The method of moments with pulse basis functions is used to solve the integral equations. This method differs from previous work in that the calculation of resistance and inductance is based on power dissipation and stored magnetic energy, rather than on impedance ratios. It will therefore be more easily extended to structures where non-TEM propagation can occur.

For the intermediate frequency range, where the conductors are on the order of the skin depth, we found it very efficient to interpolate between the results of the cross-

section and surface methods. The interpolation function was based on the average size of the conductors, measured in skin depths, and was of the form  $1/(1 + 0.16a^2/\delta^4)$ , where  $a$  is the average cross-section of the conductors, and  $\delta$  is the skin depth.

**PUBLICATIONS SUPPORTED BY ONR CONTRACT N00014-90-J-1002**

Simulation of electromagnetic radiation and scattering using a finite difference-time domain technique (K. Li, M. A. Tassoudji, R. T. Shin, and J. A. Kong), *Computer Applications in Engineering Education*, Vol. 1, No. 1, 45-63, September/October 1992.

Time domain modeling of impedance boundary condition (C. F. Lee, R. T. Shin, and J. A. Kong), *IEEE Transactions on Microwave Theory and Techniques*, Vol. 40, No. 9, September 1992.

Inverse scattering view of modal structures in inhomogeneous optical waveguides (J. Xia, A. K. Jordan, and J. A. Kong), *Journal of Optical Society of America, A*, Vol. 9, No. 5, 1992.

Electromagnetic radiation from a VLSI package and heatskin configuration (S. Y. Poh, C. F. Lee, K. Li, R. T. Shin, and J. A. Kong), submitted to *IEEE 1991 International Symposium on Electromagnetic Compatibility*, Hyatt Cherry Hill, Cherry Hill, NJ, August 13 - 15, 393 - 398, 1991.

A hybrid method of the calculation of resistance and inductance of transmission lines with arbitrary cross section (M. J. Tsuk and J. A. Kong), *IEEE Transactions on Microwave Theory and Techniques*, Vol. 39, No. 8, 1338-1347, 1991.

Analysis of diffraction from chiral gratings (S. H. Yueh and J. A. Kong), *Journal of Electromagnetic Waves and Applications*, Vol. 5, No. 7, 701-714, 1991.

Current distribution, resistance, and inductance for superconducting strip transmission lines (D. M. Sheen, S. M. Ali, D. E. Oates, R. S. Withers, and J. A. Kong), *IEEE Trans. on Applied Superconductivity*, Vol. 1, No. 2, 108-115, June, 1991.

Dyadic Green's functions in a planar stratified, arbitrarily magnetized linear plasma (T. M. Habashy, S. M. Ali, J. A. Kong, and M. D. Grossi), *Radio Science*, Vol. 26, No. 3, 701-716, May - June, 1991.

Electromagnetic calculation of soft x-ray diffraction from 0.1- $\mu\text{m}$ -scale gold structures (M. L. Schatenburg, K. Li, R. T. Shin, J. A. Kong, D. B. Olster, and H. I. Smith), *Journal of Vacuum Science and Technology* as part of the proceedings of the 35th International Symposium on Electron, Ion, and Photon Beams (paper E84), Seattle, Washington, 1-8, May 28-31, 1991.

Modelling of lossy microstrip lines with finite thickness (J. F. Kiang, S. M. Ali and J. A. Kong), *Progress in Electromagnetics Research*, No. 4, 85-116, Elsevier Publishing Company, 1991.

Input impedance of a probe-fed stacked circular microstrip antenna (A. Tulintseff, S.

Ali, and J. A. Kong) *IEEE Transactions on Antennas and Propagation*, Vol. 39, No. 3, 381–390, March 1991.

The propagation characteristics of signal lines with crossing strips in multilayered anisotropic media (C. M. Lam, S. M. Ali, and J. A. Kong), *Journal of Electromagnetic Waves and Application*, Vol. 4, No. 10, 1005–1021, 1990.

Office of Naval Research

DISTRIBUTION LIST

Arthur K. Jordan  
Scientific Officer

3 copies

Code: 1114SE  
Office of Naval Research  
800 North Quincy Street  
Arlington, VA 22217

Administrative Contracting Officer  
E19-628  
Massachusetts Institute of Technology  
Cambridge, MA 02139

1 copy

Director  
Naval Research Laboratory  
Washington, DC 20375  
Attn: Code 2627

1 copy

Defense Technical Information Center  
Bldg. 5, Cameron Station  
Alexandria, VA 22314

2 copies

# Simulation of Electromagnetic Radiation and Scattering Using a Finite Difference-Time Domain Technique

K. LI, M. A. TASSOUDJI, R. T. SHIN, and J. A. KONG

*Department of Electrical Engineering and Computer Science and Research Laboratory of Electronics, Massachusetts Institute of Technology, Cambridge, Massachusetts 02139*

## ABSTRACT

The finite difference-time domain (FD-TD) technique is applied to the solution of Maxwell's equations. A computer program, which can be used to simulate and study numerous electromagnetic phenomena, is developed and implemented on an IBM 386 compatible personal computer. The FD-TD technique is a useful tool for students in electromagnetics. The technique is flexible and can be applied to many basic EM scattering and radiation problems. Because field solutions are found as a function of time, visualization of the propagation of the EM fields is possible. The FD-TD technique is implemented for a two-dimensional rectangular grid in conjunction with a second-order absorbing boundary condition. Both E- and H-field polarizations are analyzed. Finite objects consisting of dielectric, magnetic and conducting materials, and perfectly conducting infinite ground planes are modeled. Plane wave and line current sources are implemented. In addition to the capability of animating the propagation of the EM fields, radiation and scattering patterns can be generated. © 1992 John Wiley & Sons, Inc.

## 1. INTRODUCTION

Tools which students can use as aids for understanding and visualizing electromagnetics are scarce. In an attempt to develop such a tool, the finite difference-time domain (FD-TD) technique is used to solve Maxwell's equations [1-8]. This method is especially suited for visualizing electromagnetic

phenomena, since electric and magnetic fields are calculated everywhere within a computational domain as a function of time. Thus, it is possible to observe how electromagnetic fields propagate through space with time. By facilitating the visualization of various electromagnetic phenomena, the FD-TD code can be very useful in developing intuition regarding electromagnetics.

The first step in applying the FD-TD technique involves approximating Maxwell's equations in differential form by center differences in space and time. The locations at which electric and magnetic fields are calculated are positioned on some sort of

Computer Applications in Engineering Education, Vol. 1(1) 45-63 (September/October 1992)

© 1992 John Wiley & Sons, Inc. CCC 1060-3773/92/010045-19

grid. For two-dimensional problems, two typical grids are a rectangular [1] and a triangular mesh [4]. A significant advantage of using rectangular grids over triangular grids is greater simplicity. However, since the scattering object is discretized on a rectangular grid, curves and slanted lines are approximated by staircases.

To begin the FD-TD simulation, all the fields within the computational domain are initially set to zero. At each time step, the electric fields are calculated in terms of the electric and magnetic fields of the previous time step using the difference equations obtained earlier from Maxwell's equations. Next, the magnetic fields are calculated in a similar manner. Boundary conditions are enforced at the outer boundary of the computational domain and at all dielectric and conducting interfaces. At the outer boundary, a second-order absorbing boundary condition is utilized in order to simulate unbounded space beyond the computational domain [9]. The tangential electric fields are set to zero at the conducting surfaces, and the tangential electric and magnetic fields are kept continuous at the dielectric/magnetic boundaries. The implementation of the excitation source typically requires that certain electric and magnetic fields be updated at each time step. These steps are essentially repeated until steady state is reached for a sinusoidal excitation, or until all the transient scattered fields have propagated out of the computational domain for a Gaussian pulse excitation.

In order to keep the program simple, only two-dimensional problems are examined using a uniform rectangular grid. Despite the fact that only two-dimensional geometries are considered, valuable insight can be gained through the observation of FD-TD simulations of electromagnetic phenomena. Also, in order to allow wide distribution of this program, the program is written for IBM 386 compatible personal computers. Both electric and magnetic field polarizations are implemented and examined. Scatterers can have arbitrary geometries of finite size, which consist of perfect conductors, dielectrics with finite conductivity, and magnetic materials with finite magnetic conductivity. In addition, perfectly conducting infinite ground planes are considered. The excitation sources include plane waves, and single or multiple line current sources. These excitation sources can be either sinusoidal or Gaussian pulses in time. Since field values are calculated everywhere within the computational domain, they can be stored and displayed using color plots. By displaying the fields for sequential time steps in rapid succession, the propagation of the fields can be an-

imated. By storing tangential electric and magnetic field values over a closed surface enclosing the scatterer, it is possible to calculate radiation patterns using Huygens' principle.

## 2. FINITE DIFFERENCE-TIME DOMAIN TECHNIQUE

### 2.1. Maxwell's Equations in Rectangular Coordinates

In implementing the finite difference-time domain technique, Maxwell's equations must be discretized in space and time. In this case, Yee's lattice, which is a rectangular grid, is utilized because of its simplicity [1]. Maxwell's equations in vector differential form in an isotropic and homogeneous dielectric and magnetic material are:

$$\nabla \times \bar{E} = -\frac{\partial \bar{B}}{\partial t} - \sigma_m \bar{H} \quad (1)$$

$$\nabla \times \bar{H} = \frac{\partial \bar{D}}{\partial t} + \sigma \bar{E} \quad (2)$$

$$\nabla \cdot \bar{D} = \rho \quad (3)$$

$$\nabla \cdot \bar{B} = 0 \quad (4)$$

and the constitutive relations are:

$$\bar{B} = \mu \bar{H} = \mu_r \mu_0 \bar{H} \quad (5)$$

$$\bar{D} = \epsilon \bar{E} = \epsilon_r \epsilon_0 \bar{E} \quad (6)$$

where  $\mu_r$  and  $\epsilon_r$  are relative permeability and permittivity, and  $\sigma$  and  $\sigma_m$  are electric and magnetic conductivities, respectively. Maxwell's divergence equations, (3) and (4), are satisfied in the finite difference scheme by applying appropriate initial and boundary conditions. The actual difference equations used in the FD-TD technique are based upon Maxwell's curl equations, (1) and (2), and the constitutive relations, (5) and (6).

In a rectangular coordinate system, Equations (1), (2), (5), and (6) can be written as the following set of scalar equations,

$$\mu_r \mu_0 \frac{\partial H_x}{\partial t} = \frac{\partial E_y}{\partial z} - \frac{\partial E_z}{\partial y} - \sigma_m H_x \quad (7)$$

$$\mu_r \mu_0 \frac{\partial H_y}{\partial t} = \frac{\partial E_z}{\partial x} - \frac{\partial E_x}{\partial z} - \sigma_m H_y \quad (8)$$

$$\mu_r \mu_0 \frac{\partial H_z}{\partial t} = \frac{\partial E_x}{\partial y} - \frac{\partial E_y}{\partial x} - \sigma_m H_z \quad (9)$$

$$\epsilon_r \epsilon_0 \frac{\partial E_x}{\partial t} = \frac{\partial H_z}{\partial y} - \frac{\partial H_y}{\partial z} - \sigma E_x \quad (10)$$

$$\epsilon_r \epsilon_0 \frac{\partial E_y}{\partial t} = \frac{\partial H_x}{\partial z} - \frac{\partial H_z}{\partial x} - \sigma E_y \quad (11)$$

$$\epsilon_r \epsilon_0 \frac{\partial E_z}{\partial t} = \frac{\partial H_y}{\partial x} - \frac{\partial H_x}{\partial y} - \sigma E_z \quad (12)$$

For two-dimensional problems, which are assumed to be uniform and infinite in the  $y$  direction, all the partial derivatives with respect to  $y$  are equal to zero. Maxwell's equations in arbitrary homogeneous, isotropic media, for two-dimensional problems in a rectangular coordinate system, decouple into the  $H$ -field polarization,

$$\mu_r \mu_0 \frac{\partial H_y}{\partial t} = \frac{\partial E_z}{\partial x} - \frac{\partial E_x}{\partial z} - \sigma_m H_y \quad (13)$$

$$\epsilon_r \epsilon_0 \frac{\partial E_x}{\partial t} = -\frac{\partial H_y}{\partial z} - \sigma E_x \quad (14)$$

$$\epsilon_r \epsilon_0 \frac{\partial E_z}{\partial t} = \frac{\partial H_y}{\partial x} - \sigma E_z \quad (15)$$

and the  $E$ -field polarization,

$$\epsilon_r \epsilon_0 \frac{\partial E_y}{\partial t} = \frac{\partial H_x}{\partial z} - \frac{\partial H_z}{\partial x} - \sigma E_y \quad (16)$$

$$\mu_r \mu_0 \frac{\partial H_x}{\partial t} = \frac{\partial E_y}{\partial z} - \sigma_m H_x \quad (17)$$

$$\mu_r \mu_0 \frac{\partial H_z}{\partial t} = -\frac{\partial E_y}{\partial x} - \sigma_m H_z \quad (18)$$

In free space, where  $\epsilon_r = \mu_r = 1$  and  $\sigma = \sigma_m = 0$ , Equations (13)–(18) simplify to

$$\mu_0 \frac{\partial H_y}{\partial t} = \frac{\partial E_z}{\partial x} - \frac{\partial E_x}{\partial z} \quad (19)$$

$$\epsilon_0 \frac{\partial E_x}{\partial t} = -\frac{\partial H_y}{\partial z} \quad (20)$$

$$\epsilon_0 \frac{\partial E_z}{\partial t} = \frac{\partial H_y}{\partial x} \quad (21)$$

for the  $H$ -field polarization and

$$\epsilon_0 \frac{\partial E_y}{\partial t} = \frac{\partial H_x}{\partial z} - \frac{\partial H_z}{\partial x} \quad (22)$$

$$\mu_0 \frac{\partial H_x}{\partial t} = \frac{\partial E_y}{\partial z} \quad (23)$$

$$\mu_0 \frac{\partial H_z}{\partial t} = -\frac{\partial E_y}{\partial x} \quad (24)$$

for the  $E$ -field polarization.

The following notation for any function of time and space will be used in the finite difference equations,

$$f(i\Delta x, k\Delta z, n\Delta t) = f^n(i, k) \quad (25)$$

The partial derivatives in space and time, within Maxwell's equations, are approximated using center differences,

$$\frac{\partial f(\xi)}{\partial \xi} \approx \frac{f(\xi + \Delta\xi/2) - f(\xi - \Delta\xi/2)}{\Delta\xi} \quad (26)$$

The electric and magnetic field components are interlaced in time, and are calculated in a leap-frog manner (i.e., first the electric fields are calculated, then the magnetic fields are calculated, and the sequence is repeated). The electric and magnetic field components are interlaced spatially a half-grid cell apart.

Only the  $H$ -field polarization will be treated explicitly because the  $E$ -field polarization can be treated easily through the use of duality.

## 2.2. Finite Difference Equations for the H-Field Polarization

**2.2.1. Treatment of Free Space.** For the  $H$ -field polarization, the finite difference equations in free space are obtained by applying center differences to Equations (19)–(21).

$$\begin{aligned} & H_y^{n+1/2} \left( i + \frac{1}{2}, k + \frac{1}{2} \right) \\ &= H_y^{n-1/2} \left( i + \frac{1}{2}, k + \frac{1}{2} \right) + \frac{1}{\eta_0} \frac{\Delta\tau}{\Delta x} \\ &\quad \times \left[ E_z^n \left( i + 1, k + \frac{1}{2} \right) - E_z^n \left( i, k + \frac{1}{2} \right) \right] \\ &\quad - \frac{1}{\eta_0} \frac{\Delta\tau}{\Delta z} \left[ E_x^n \left( i + \frac{1}{2}, k + 1 \right) \right. \\ &\quad \left. - E_x^n \left( i + \frac{1}{2}, k \right) \right] \end{aligned} \quad (27)$$

$$\begin{aligned}
E_x^{n+1}\left(i + \frac{1}{2}, k\right) &= E_x^n\left(i + \frac{1}{2}, k\right) \left(\frac{2\epsilon_r - \sigma\eta_0\Delta\tau}{2\epsilon_r + \sigma\eta_0\Delta\tau}\right) \\
E_x^{n+1}\left(i + \frac{1}{2}, k\right) &= E_x^n\left(i + \frac{1}{2}, k\right) \\
&\quad - \eta_0 \frac{\Delta\tau}{\Delta z} \left[ H_y^{n+1/2}\left(i + \frac{1}{2}, k + \frac{1}{2}\right) \right. \\
&\quad \left. - H_y^{n+1/2}\left(i + \frac{1}{2}, k - \frac{1}{2}\right) \right] \quad (28)
\end{aligned}$$

$$\begin{aligned}
E_z^{n+1}\left(i, k + \frac{1}{2}\right) &= E_z^n\left(i, k + \frac{1}{2}\right) \\
&\quad + \eta_0 \frac{\Delta\tau}{\Delta x} \left[ H_y^{n+1/2}\left(i + \frac{1}{2}, k + \frac{1}{2}\right) \right. \\
&\quad \left. - H_y^{n+1/2}\left(i - \frac{1}{2}, k + \frac{1}{2}\right) \right] \quad (29)
\end{aligned}$$

where

$$\eta_0 = \sqrt{\frac{\mu_0}{\epsilon_0}} \quad (30)$$

$$\Delta\tau = c\Delta t = \frac{\Delta t}{\sqrt{\mu_0\epsilon_0}} \quad (31)$$

The locations of the field components on a unit cell of the rectangular grid for the  $H$ -field polarization are shown in Figure 1.

**2.2.2. Treatment of Dielectric and Magnetic Material.** The finite difference equations in an isotropic, homogeneous, dielectric, and magnetic material

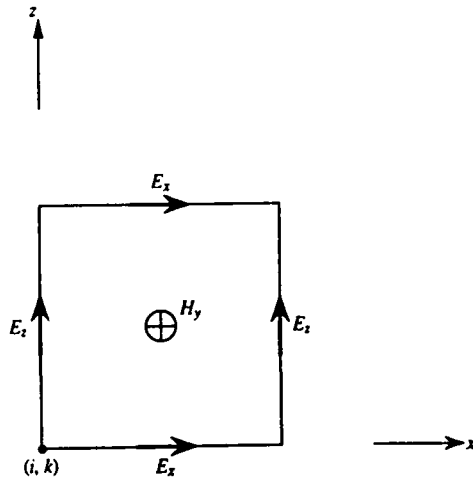


Figure 1 Field Locations on Rectangular Grid for  $H$ -Field Polarization.

are obtained by discretizing Equations (13)–(15) for the  $H$ -field polarization. The derivatives are replaced by center differences, and the electric- and magnetic-field terms involving electric and magnetic conductivities are approximated by using an average of the field values at a half time step before and after the desired time.

$$\begin{aligned}
H_y^{n+1/2}\left(i + \frac{1}{2}, k + \frac{1}{2}\right) &= H_y^{n-1/2}\left(i + \frac{1}{2}, k + \frac{1}{2}\right) \\
&\quad \times \left(\frac{2\mu_r - \sigma_m\Delta\tau/\eta_0}{2\mu_r + \sigma_m\Delta\tau/\eta_0}\right) \\
&\quad + \frac{1}{\eta_0} \left[ \frac{2\Delta\tau}{(2\mu_r + \sigma_m\Delta\tau/\eta_0)} \right] \\
&\quad \times \left\{ \left[ E_z^n\left(i + 1, k + \frac{1}{2}\right) \right. \right. \\
&\quad \left. \left. - E_z^n\left(i, k + \frac{1}{2}\right) \right] / \Delta x \right. \\
&\quad \left. - \left[ E_x^n\left(i + \frac{1}{2}, k + 1\right) \right. \right. \\
&\quad \left. \left. - E_x^n\left(i + \frac{1}{2}, k\right) \right] / \Delta z \right\} \quad (32)
\end{aligned}$$

$$\begin{aligned}
E_x^{n+1}\left(i + \frac{1}{2}, k\right) &= E_x^n\left(i + \frac{1}{2}, k\right) \left(\frac{2\epsilon_r - \sigma\eta_0\Delta\tau}{2\epsilon_r + \sigma\eta_0\Delta\tau}\right) \\
&\quad - \eta_0 \left[ \frac{2\Delta\tau}{\Delta z(2\epsilon_r + \sigma\eta_0\Delta\tau)} \right] \\
&\quad \times \left[ H_y^{n+1/2}\left(i + \frac{1}{2}, k + \frac{1}{2}\right) \right. \\
&\quad \left. - H_y^{n+1/2}\left(i + \frac{1}{2}, k - \frac{1}{2}\right) \right] \quad (33)
\end{aligned}$$

$$\begin{aligned}
E_z^{n+1}\left(i, k + \frac{1}{2}\right) &= E_z^n\left(i, k + \frac{1}{2}\right) \left(\frac{2\epsilon_r - \sigma\eta_0\Delta\tau}{2\epsilon_r + \sigma\eta_0\Delta\tau}\right) \\
&\quad + \eta_0 \left[ \frac{2\Delta\tau}{\Delta x(2\epsilon_r + \sigma\eta_0\Delta\tau)} \right] \\
&\quad \times \left[ H_y^{n+1/2}\left(i + \frac{1}{2}, k + \frac{1}{2}\right) \right. \\
&\quad \left. - H_y^{n+1/2}\left(i - \frac{1}{2}, k + \frac{1}{2}\right) \right] \quad (34)
\end{aligned}$$

**2.2.3. Treatment of Interfaces Between Two Media.** The interface between any two media always occurs at integer nodes  $(i, k)$  (Figure 2). At the interface between two dielectric and magnetic materials, the finite difference equation for the tangential electric field (i.e.,  $E_x$ ) must be treated carefully (Figure 3). Using the integral form of Equation (2) to calculate the electric field tangential to the interface,  $E_x$ , yields

$$\begin{aligned} \oint_C \vec{H} \cdot d\vec{l} &= \iint_{S_1+S_2} \left( \frac{\partial \vec{D}}{\partial t} + \sigma \vec{E} \right) \cdot d\vec{S} \\ &= \iint_{S_1} \left( \epsilon_1 \frac{\partial \vec{E}}{\partial t} + \sigma_1 \vec{E} \right) \cdot d\vec{S} \quad (35) \\ &\quad + \iint_{S_2} \left( \epsilon_2 \frac{\partial \vec{E}}{\partial t} + \sigma_2 \vec{E} \right) \cdot d\vec{S} \end{aligned}$$

Changing Equation (35) to a finite difference equation yields

$$\begin{aligned} E_x^{n+1} \left( i + \frac{1}{2}, k \right) &= E_x^n \left( i + \frac{1}{2}, k \right) \\ &\times \left[ \frac{2(\epsilon_{r1} + \epsilon_{r2}) - (\sigma_1 + \sigma_2)\eta_0\Delta\tau}{2(\epsilon_{r1} + \epsilon_{r2}) + (\sigma_1 + \sigma_2)\eta_0\Delta\tau} \right] \\ &- \eta_0 \left[ \frac{4\Delta\tau/\Delta z}{2(\epsilon_{r1} + \epsilon_{r2}) - (\sigma_1 + \sigma_2)\eta_0\Delta\tau} \right] \\ &\times \left[ H_y^{n+1/2} \left( i + \frac{1}{2}, k + \frac{1}{2} \right) \right. \\ &\quad \left. - H_y^{n+1/2} \left( i + \frac{1}{2}, k - \frac{1}{2} \right) \right] \quad (36) \end{aligned}$$

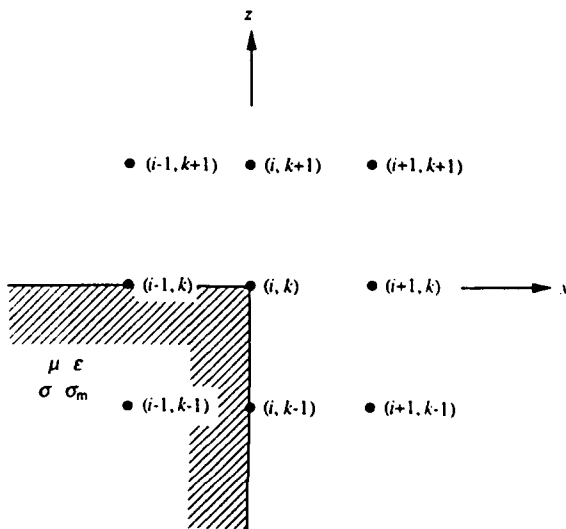


Figure 2 Positioning of a Media on the Rectangular Grid.

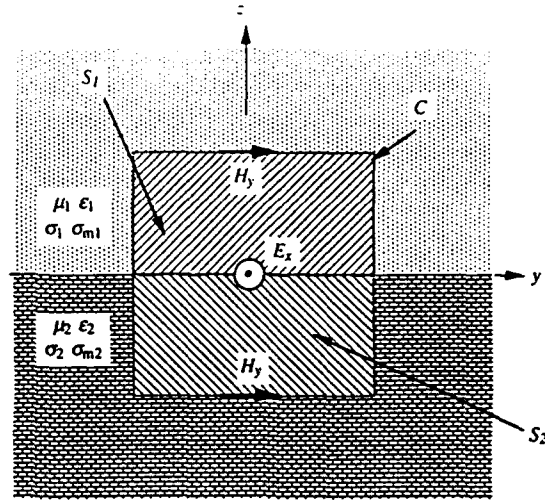


Figure 3 Interface Between Two Dielectric and Magnetic Media for  $H$ -Field Polarization.

**2.2.4. Treatment of Perfect Electric Conductor.** The boundary condition at perfect electric conductors states that the tangential electric field must be zero.

$$\hat{n} \times \vec{E} = 0 \quad (37)$$

The field locations for the  $H$ -field polarization with respect to the integer nodes  $(i, k)$  are shown in Figure 1. From Figures 1 and 2, it is clear that the electric fields, which are calculated at points on the surface of the perfect electric conductor, are always tangential to the surface. Thus, in the finite difference-time domain scheme, the boundary condition at the perfect electric conductor can be satisfied by simply setting these electric fields equal to zero at each time step.

**2.2.5. Treatment of Perfect Magnetic Conductor.** At a perfect magnetic conductor, the tangential magnetic field must be zero, i.e.,

$$\hat{n} \times \vec{H} = 0 \quad (38)$$

This boundary condition is satisfied when the tangential electric field at the surface of the perfect magnetic conductor is calculated. One way of obtaining a difference equation for the tangential electric field (i.e.,  $E_x$ ) is to simplify the original problem (Figure 4) by using image theory (Figure 5). The difference equation for  $E_x$  at the interface between a perfect magnetic conductor and a dielectric and magnetic material is given by

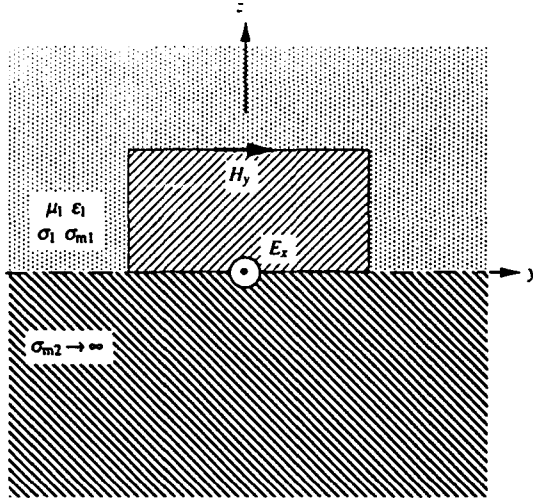


Figure 4 Interface Between a Media and a Perfect Magnetic Conductor.

$$\begin{aligned}
 E_x^{n+1} \left( i + \frac{1}{2}, k \right) &= E_x^n \left( i + \frac{1}{2}, k \right) \left( \frac{2\epsilon_r - \sigma\eta_0\Delta\tau}{2\epsilon_r + \sigma\eta_0\Delta\tau} \right) \\
 &\quad - \eta_0 \left[ \frac{2\Delta\tau}{\Delta z (2\epsilon_r + \sigma\eta_0\Delta\tau)} \right] \\
 &\quad 2H_y^{n+1/2} \times \left( i + \frac{1}{2}, k + \frac{1}{2} \right)
 \end{aligned} \quad (39)$$

The implementation of perfect magnetic conductors is of particular importance. By duality, the perfect magnetic conductor for the  $H$ -field polarization becomes the perfect electric conductor for the  $E$ -field polarization.

### 2.3. Finite Difference Equations for the $E$ -Field Polarization

All the difference equations needed for the  $E$ -field polarization can be easily obtained through the use of duality. The difference equations used for the  $H$ -field polarization can be directly applied for the  $E$ -field polarization with the following substitutions,

$$\vec{E} \rightarrow \vec{H} \quad (40)$$

$$\vec{H} \rightarrow -\vec{E} \quad (41)$$

$$\mu_0 \rightarrow \epsilon_0 \quad (42)$$

$$\epsilon_0 \rightarrow \mu_0 \quad (43)$$

$$\eta_0 \rightarrow 1/\eta_0 \quad (44)$$

$$\mu_r \rightarrow \epsilon_r \quad (45)$$

$$\epsilon_r \rightarrow \mu_r \quad (46)$$

$$\sigma \rightarrow \sigma_m \quad (47)$$

$$\sigma_m \rightarrow \sigma \quad (48)$$

All other variables remain the same.

### 2.4. Stability and Accuracy

The choices of  $\Delta x$ ,  $\Delta z$ , and  $\Delta\tau$ , are motivated by reasons of accuracy and stability [3, 6]. In general, to obtain accurate results,  $\Delta x$  and  $\Delta z$  must be a small fraction ( $\sim \frac{1}{10}$ ) of the smallest wavelength in any media expected in the model or of the smallest dimension of the scatterer. For this problem, the spacing in the  $x$  and  $z$  directions will be equal in size,

$$\Delta x = \Delta z = \Delta \quad (49)$$

To ensure the stability of this time-stepping algorithm,  $\Delta\tau$  must satisfy the following condition [3].

$$\Delta\tau \leq \left( \frac{1}{\Delta x^2} + \frac{1}{\Delta z^2} \right)^{-1/2} = \frac{1}{\sqrt{2}} \Delta \quad (50)$$

### 2.5. Implementation of Excitation Source

The two basic types of sources, which are plane waves and line current sources, are treated differ-

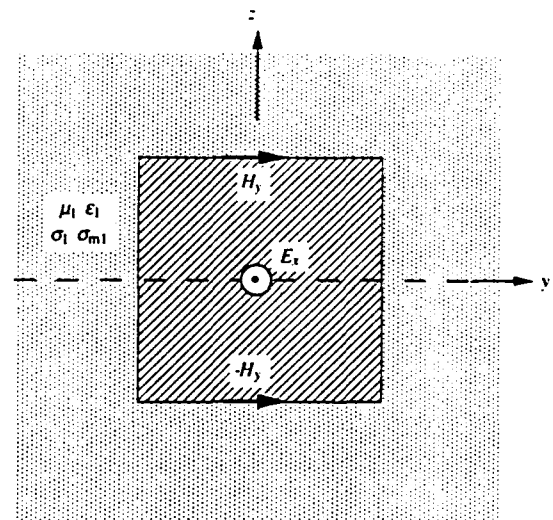


Figure 5 Image Problem of Interface Between a Media and a Perfect Magnetic Conductor.

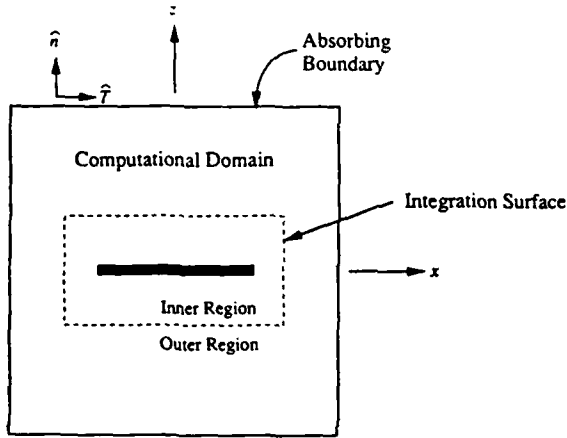


Figure 6 Absorbing Boundary, Computational Domain and Closed Surface on Which Fields are Sampled With a Finite Scatterer.

ently. When the excitation source is assumed to be either a sinusoidal or Gaussian pulse plane wave, the computational domain is separated into two regions in order to facilitate the treatment of the excitation source (Figures 6 and 7).

For a finite scatterer, within the inner region, total fields are calculated, while in the outer region, only scattered fields are calculated. The scattered fields are defined to be the difference between the total fields and the incident plane wave.

$$\vec{H}_s(x, z, t) = \vec{H}_t(x, z, t) - \vec{H}_i(x, z, t) \quad (51)$$

$$\vec{E}_s(x, z, t) = \vec{E}_t(x, z, t) - \vec{E}_i(x, z, t) \quad (52)$$

The incident fields are subtracted from field quantities just within the inner regions, when they are used to calculate field quantities just beyond the

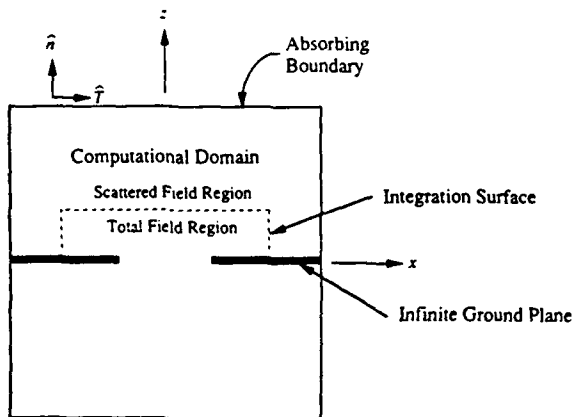


Figure 7 Absorbing Boundary, Computational Domain and Surface on Which Fields are Sampled With an Infinite Ground Plane Geometry.

inner region. The incident fields are added to field quantities just outside the inner regions, when they are used to calculate field quantities just within the inner region [10].

For the  $H$ -field polarization, some sample finite difference equations in the vicinity of the interface between the two regions are (Figure 8):

$$\begin{aligned} & H_{sv}^{n+1/2} \left( i + \frac{1}{2}, k + \frac{1}{2} \right) \\ &= H_{sv}^{n-1/2} \left( i + \frac{1}{2}, k + \frac{1}{2} \right) \\ &+ \frac{1}{\eta_0} \frac{\Delta \tau}{\Delta x} \left[ E_{sz}^n \left( i + 1, k + \frac{1}{2} \right) \right. \\ &- \left. E_{sz}^n \left( i, k + \frac{1}{2} \right) \right] \\ &- \frac{1}{\eta_0} \frac{\Delta \tau}{\Delta z} \left\{ E_{sv}^n \left( i + \frac{1}{2}, k + 1 \right) \right. \\ &- \left. \left[ E_{iv}^n \left( i + \frac{1}{2}, k \right) - E_{iv}^n \left( i + \frac{1}{2}, k \right) \right] \right\} \\ & E_{iv}^{n+1} \left( i + \frac{1}{2}, k \right) = E_{iv}^n \left( i + \frac{1}{2}, k \right) \\ &- \eta_0 \frac{\Delta \tau}{\Delta z} \left\{ \left[ H_{sv}^{n+1/2} \left( i + \frac{1}{2}, k + \frac{1}{2} \right) \right. \right. \\ &+ \left. \left. H_{iv}^{n+1/2} \left( i + \frac{1}{2}, k + \frac{1}{2} \right) \right] \right. \\ &- \left. \left. H_{iv}^{n+1/2} \left( i + \frac{1}{2}, k - \frac{1}{2} \right) \right] \right\} \end{aligned} \quad (54)$$

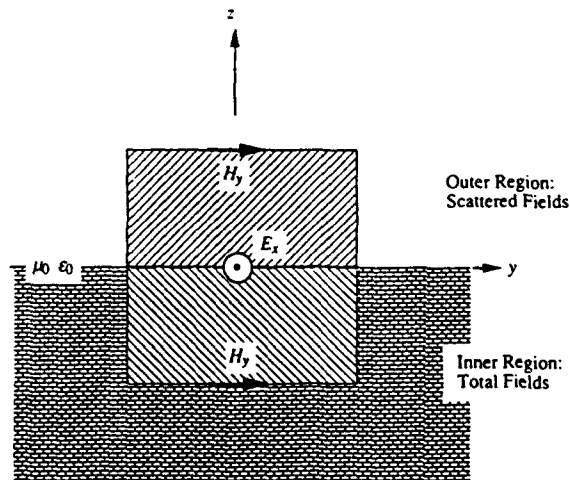


Figure 8 Interface Between Inner and Outer Regions.

$$\begin{aligned}
 E_{xz}^{n+1}\left(i, k + \frac{1}{2}\right) &= E_{xz}^n\left(i, k + \frac{1}{2}\right) + \eta_0 \frac{\Delta\tau}{\Delta x} \\
 &\times \left[ H_{xy}^{n+1/2}\left(i + \frac{1}{2}, k + \frac{1}{2}\right) \right. \\
 &\quad \left. - H_{xy}^{n+1/2}\left(i - \frac{1}{2}, k + \frac{1}{2}\right) \right]
 \end{aligned} \quad (55)$$

For an infinite ground plane configuration, the computational domain is basically divided into the region above the ground plane and the region below the ground plane. For plane-wave illumination from the upper half space, total fields are calculated in the lower region, while in the upper region, only scattered fields are calculated. In this case, the scattered fields are defined to be the total fields minus the incident plane wave and the plane wave that would have been reflected from a uniform infinite ground plane.

$$\begin{aligned}
 \bar{H}_y(x, z, t) &= \bar{H}_t(x, z, t) \\
 &\quad - \bar{H}_i(x, z, t) - \bar{H}_r(x, z, t)
 \end{aligned} \quad (56)$$

$$\begin{aligned}
 \bar{E}_z(x, z, t) &= \bar{E}_t(x, z, t) \\
 &\quad - \bar{E}_i(x, z, t) - \bar{E}_r(x, z, t)
 \end{aligned} \quad (57)$$

The removal of the reflected plane wave from the upper half space is essential, because the reflected plane wave is infinite in size and could not otherwise be adequately modeled within the finite computational domain. For plane-wave illumination from the lower half space the total and scattered fields are simply calculated in the opposite regions. The implementation of a plane wave is basically identical to the implementation for a finite scatterer, except with the slightly different definition of the scattered field.

The implementation of line current sources is straightforward. In this situation, total fields are calculated within the entire computational domain. Line current sources are essentially point sources in this two-dimensional simulation. For the  $E$ -field polarization, an electric line current in the  $y$  direction is the source, while for the  $H$ -field polarization the source is a magnetic line current in the  $y$  direction. For a sinusoidal excitation, the value of each line current source is added to the value of either  $E_y$  or  $H_y$ , depending on the polarization, at a single point at every time step. Alternatively, for a Gaussian pulse excitation, the value of the appropriate field component is set to be equal to the line current source. The advantage of adding field values instead of imposing field values is that fields can propagate

through the current source. The advantage of imposing field values is that the value of the field at that point is known for all time.

The actual amplitude of the current is not strictly determined by the amplitude of the adjustment to a field quantity at a particular node. The fields near a point source are singular. Thus, in this FD-TD scheme, the adjustment of a field value at a single point does not correspond to a two-dimensional point source (i.e., a line current source with zero cross section), rather this implementation more accurately models a line current source with a finite nonzero cross section. One way of obtaining the amplitude of the line current source is by performing some sort of calibration [8]. In particular, the prediction obtained using the FD-TD scheme with a particular grid spacing, for the power radiated by a line current source in free space, can be compared to the closed-form solution. The power radiated in the FD-TD scheme can be obtained by integrating the time-average Poynting power density over some closed surface. The time-average Poynting power density can be found from the electric and magnetic fields produced by the FD-TD simulation. The amplitude of the field quantity added at a single point for a particular grid spacing can be related to the amplitude of the current in the line source. This calibration factor will, in general, be a function of the grid spacing [8]. This calibration factor is also applicable to line current sources which interact with each other and/or arbitrary media, so long as the grid spacing, which is used, is the same as the spacing used in performing the calibration.

The presence of reactive fields generated by a line current source, which decay rapidly further away from the source, can cause inaccuracies in calculating field values in the vicinity of the line source [7]. Hence, interaction between a line current source and some arbitrary media may not be adequately modeled when the media is close enough to be affected by the reactive fields generated by the line current source. One simple remedy to this problem involves using a finer mesh in the vicinity of the line current source [7].

## 2.6. Absorbing Boundary Condition

An absorbing boundary condition (ABC) at the outer boundary is needed to make the computational domain finite, and to simulate unbounded space beyond the computational domain (Figures 6 and 7) [9–12]. The absorbing boundary condition used for this problem is the second-order approximation derived by Engquist and Majda [9],

$$\left( \frac{\partial^2}{\partial n \partial \tau} + \frac{\partial^2}{\partial \tau^2} - \frac{1}{2} \frac{\partial^2}{\partial T^2} \right) w = 0 \quad (58)$$

where  $w$  is a field quantity which is tangential to the absorbing boundary,  $\hat{n}$  is the normal direction,  $\hat{T}$  is the tangential direction, and  $\tau$  is time normalized with respect to the speed of light. The second-order ABC works very well for waves which are at or near normal incidence, and not as well for waves which are incident at grazing angles. This second-order ABC can be applied to all the edges of the computational domain, except in the vicinity of any media other than free space which extends beyond the computational domain.

At the outer boundary and within or next to a media other than free space, a first-order ABC is used, since the fields may not be continuous across the material interfaces. This program was intended for use with infinite perfectly conducting planes, where the tangential electric or magnetic fields are discontinuous. The presence of dielectric or magnetic materials at the outer boundary may not be adequately treated with the use of this first-order ABC. The first-order ABC is characterized by the following equation,

$$\left( \frac{\partial}{\partial n} + \frac{\partial}{\partial \tau} \right) w = 0 \quad (59)$$

where  $\hat{n}$  is the normal direction. In order to simplify the implementation of the first-order absorbing boundary, Equation (59) is differentiated with respect to time, yielding

$$\left( \frac{\partial^2}{\partial n \partial \tau} + \frac{\partial^2}{\partial \tau^2} \right) w = 0 \quad (60)$$

Equation (60) is equal to Equation (58) without the tangential components.

At the corners of the computational domain, the second-order ABC cannot be used, since the normal and tangential directions are not defined. In treating the corners, an average of the two limiting cases for the normal direction is used with a first-order ABC,

$$\frac{1}{2} \left[ \left( \frac{\partial}{\partial n_1} + \frac{\partial}{\partial \tau} \right) + \left( \frac{\partial}{\partial n_2} + \frac{\partial}{\partial \tau} \right) \right] w = 0 \quad (61)$$

where  $\hat{n}_1$ , and  $\hat{n}_2$  are the two limiting cases for the normal direction at the corner. This equation is also differentiated with respect to time so that the equation has the same form as the second-order ABC. The ABC at the corners is not as important as at

the edges, because there is only one point at each corner, while there are many points on the edges. Thus, in general, using the first-order ABC at the corners will not cause significant deterioration in the accuracy of the algorithm.

For the  $H$ -field polarization, the absorbing boundary conditions are applied to the magnetic field,  $H_y$ . Applying center differences to Equation (58) for the  $+z$  boundary  $\left( k = K^+ + \frac{1}{2} \right)$ , and then using temporal and spatial averages to obtain  $H_y$  at positions and times where  $H_y$  is calculated, yields

$$\begin{aligned} & H_y^{n+1/2} \left( i + \frac{1}{2}, K^+ + \frac{1}{2} \right) \\ &= -H_y^{n-3/2} \left( i + \frac{1}{2}, K^+ - \frac{1}{2} \right) \\ &+ \frac{\Delta\tau - \Delta}{\Delta\tau + \Delta} \left[ H_y^{n+1/2} \left( i + \frac{1}{2}, K^+ - \frac{1}{2} \right) \right. \\ &+ \left. H_y^{n-3/2} \left( i + \frac{1}{2}, K^+ + \frac{1}{2} \right) \right] \\ &+ \frac{2\Delta}{\Delta\tau + \Delta} \left[ H_y^{n-1/2} \left( i + \frac{1}{2}, K^+ + \frac{1}{2} \right) \right. \\ &+ \left. H_y^{n-1/2} \left( i + \frac{1}{2}, K^+ - \frac{1}{2} \right) \right] \\ &+ \frac{\Delta\tau^2}{2\Delta(\Delta\tau + \Delta)} \\ &\times \left[ H_y^{n-1/2} \left( i + \frac{3}{2}, K^+ + \frac{1}{2} \right) \right. \\ &- \left. 2H_y^{n-1/2} \left( i + \frac{1}{2}, K^+ + \frac{1}{2} \right) \right. \\ &+ \left. H_y^{n-1/2} \left( i - \frac{1}{2}, K^+ + \frac{1}{2} \right) \right. \\ &+ \left. H_y^{n-1/2} \left( i + \frac{3}{2}, K^+ - \frac{1}{2} \right) \right. \\ &- \left. 2H_y^{n-1/2} \left( i + \frac{1}{2}, K^+ - \frac{1}{2} \right) \right. \\ &+ \left. H_y^{n-1/2} \left( i - \frac{1}{2}, K^+ - \frac{1}{2} \right) \right] \end{aligned} \quad (62)$$

The difference equations satisfying the ABC for the other three edges of the computational domain have the same form, and hence, are not shown here.

The difference equation satisfying the ABC

[Equation (61)] at the  $+x, +z$  corner  $\left(i = I^+ + \frac{1}{2}, k = K^+ + \frac{1}{2}\right)$ , is

$$\begin{aligned}
& H_y^{n+1/2} \left( I^+ + \frac{1}{2}, K^+ + \frac{1}{2} \right) \\
&= \frac{1}{2} \left\{ -H_y^{n-3/2} \left( I^+ + \frac{1}{2}, K^+ - \frac{1}{2} \right) \right. \\
&\quad + \frac{\Delta\tau - \Delta}{\Delta\tau + \Delta} \left[ H_y^{n+1/2} \left( I^+ + \frac{1}{2}, K^+ - \frac{1}{2} \right) \right. \\
&\quad + H_y^{n-3/2} \left( I^+ + \frac{1}{2}, K^+ + \frac{1}{2} \right) \left. \right] \\
&\quad + \frac{2\Delta}{\Delta\tau + \Delta} \left[ H_y^{n-1/2} \left( I^+ + \frac{1}{2}, K^+ + \frac{1}{2} \right) \right. \\
&\quad + H_y^{n-1/2} \left( I^+ + \frac{1}{2}, K^+ - \frac{1}{2} \right) \left. \right] \\
&\quad - H_y^{n-3/2} \left( I^+ - \frac{1}{2}, K^+ + \frac{1}{2} \right) \\
&\quad + \frac{\Delta\tau - \Delta}{\Delta\tau + \Delta} \\
&\quad \times \left[ H_y^{n+1/2} \left( I^+ - \frac{1}{2}, K^+ + \frac{1}{2} \right) \right. \\
&\quad + H_y^{n-3/2} \left( I^+ + \frac{1}{2}, K^+ + \frac{1}{2} \right) \left. \right] \\
&\quad + \frac{2\Delta}{\Delta\tau + \Delta} \left[ H_y^{n-1/2} \left( I^+ + \frac{1}{2}, K^+ + \frac{1}{2} \right) \right. \\
&\quad \left. \left. + H_y^{n-1/2} \left( I^+ - \frac{1}{2}, K^+ + \frac{1}{2} \right) \right] \right\} \quad (63)
\end{aligned}$$

Again, the difference equations at the other three corners have the same form and are not shown.

A first-order ABC applied at the  $\pm z$  edge  $\left(k = K^+ + \frac{1}{2}\right)$  near a media which extends beyond the computational domain would have the form

$$\begin{aligned}
& H_y^{n+1/2} \left( i + \frac{1}{2}, K^+ + \frac{1}{2} \right) \\
&= -H_y^{n-3/2} \left( i + \frac{1}{2}, K^+ - \frac{1}{2} \right) \\
&\quad + \frac{\Delta\tau - \Delta}{\Delta\tau + \Delta} \left[ H_y^{n+1/2} \left( i + \frac{1}{2}, K^+ - \frac{1}{2} \right) \right.
\end{aligned} \quad (64)$$

$$\begin{aligned}
& \left. + H_y^{n-3/2} \left( i + \frac{1}{2}, K^+ + \frac{1}{2} \right) \right] \\
& + \frac{2\Delta}{\Delta\tau + \Delta} \left[ H_y^{n-1/2} \left( i + \frac{1}{2}, K^+ + \frac{1}{2} \right) \right. \\
& \left. + H_y^{n-1/2} \left( i + \frac{1}{2}, K^+ - \frac{1}{2} \right) \right]
\end{aligned}$$

The absorbing boundary is not required to absorb the incident plane wave, because the scattered fields, from which the incident plane wave has been analytically removed, are calculated outside the inner region. With infinite ground planes, the reflected plane wave is also analytically removed from the scattered field region and need not be absorbed by the absorbing boundary. Since the scattered field radiates from the scatterer, the outgoing scattered fields will not be incident on the absorbing boundary at grazing angles, which allows the ABC to absorb a large percentage of the outgoing scattered fields.

## 2.7. Limitations

While the FD-TD technique can provide very accurate predictions and solutions to various electromagnetic phenomena, there are a number of approximations inherent to the technique. The center difference approximations applied to Maxwell's equations are accurate to the second order [i.e., the error term is proportional to the square of the grid size ( $\Delta^2$ )]. This error can be kept to a minimum by choosing the grid size to be less than a tenth of the shortest wavelength of interest. Some dispersion is introduced by the discretization of Maxwell's equations (i.e., different frequency components travel at slightly different velocities). Geometries are discretized on a rectangular grid. Hence, the dimensions of any scatterer are restricted to integer multiples of the grid size, and curved surfaces must be approximated with staircases. In general, as long as the grid size is small compared to the dimensions of the scatterer, the scatterer can be adequately modeled on rectangular grids. In order to obtain absolute field quantities when line current sources are used, the sources must be calibrated. When a line source is too close to a boundary, inaccuracies may occur in the field quantities due to the inadequate modeling of the reactive fields. At the outer boundary some reflections will occur because the absorbing boundary condition is an approximate condition. These reflections can be kept tolerable by locating the outer boundary at least half a wavelength away from the scatterer [8].

### 3. CALCULATION OF RADIATION/SCATTERING PATTERNS

The calculation of the radiation or scattering patterns requires the use of Huygens' principle. Huygens' principle states that the field solution in a region is completely determined by the tangential fields on a surface which completely surrounds the region [13]. The mathematical formulation of Huygens' principle for free space in two dimensions, assuming an  $e^{-i\omega t}$  time dependence, has the following forms:

$$\begin{aligned} \bar{E}(\bar{\rho}) = \int_{S'} dS' \{ i\omega\mu_0 g(\bar{\rho}, \bar{\rho}') [\hat{n} \times \bar{H}(\bar{\rho}')] \\ + \nabla \times g(\bar{\rho}, \bar{\rho}') [\hat{n} \times \bar{E}(\bar{\rho}')] \} \end{aligned} \quad (65)$$

$$\begin{aligned} \bar{H}(\bar{\rho}) = \int_{S'} dS' \{ -i\omega\epsilon_0 g(\bar{\rho}, \bar{\rho}') [\hat{n} \times \bar{E}(\bar{\rho}')] \\ + \nabla \times g(\bar{\rho}, \bar{\rho}') [\hat{n} \times \bar{H}(\bar{\rho}')] \} \end{aligned} \quad (66)$$

where:

$$g(\bar{\rho}, \bar{\rho}') = \frac{i}{4} H_0^{(1)}(k_0 |\bar{\rho} - \bar{\rho}'|) \quad (67)$$

$$\bar{\rho} = \hat{x}x + \hat{z}z \quad (68)$$

$$\bar{\rho}' = \hat{x}x' + \hat{z}z' \quad (69)$$

$$k_0 = \omega\sqrt{\epsilon_0\mu_0} \quad (70)$$

and  $\hat{n}$  is the normal to the surface  $S'$ , and  $H_0^{(1)}$  is the zeroth-order Hankel function of the first kind.

Equations (65) and (66) are duals, so that by solving one, the other can be found by duality. Assuming that the integration surface is a rectangular box of dimensions  $2a$  in the  $x$  direction and  $2b$  in the  $z$  direction, Equation (65) becomes the following equation:

$$\begin{aligned} \bar{E}(\bar{\rho}) = -\hat{y} \frac{k_0}{4} \int_{-a}^a dx' \left\{ \eta_0 H_x(\bar{\rho}') \right. \\ \left. H_0^{(1)} \times (k_0 |\bar{\rho} - \bar{\rho}'|) - i \frac{(z - z')}{|\bar{\rho} - \bar{\rho}'|} \right. \\ \left. \times E_y(\bar{\rho}') H_1^{(1)}(k_0 |\bar{\rho} - \bar{\rho}'|) \right\} \Bigg|_{z'=-b} \\ - \left[ \eta_0 H_x(\bar{\rho}') H_0^{(1)}(k_0 |\bar{\rho} - \bar{\rho}'|) \right. \\ \left. - i \frac{(z - z')}{|\bar{\rho} - \bar{\rho}'|} E_y(\bar{\rho}') \right] \end{aligned}$$

$$\begin{aligned} \times H_1^{(1)}(k_0 |\bar{\rho} - \bar{\rho}'|) \Bigg|_{z'=b} \} \\ + \hat{y} \frac{k_0}{4} \int_{-b}^b dz' \left\{ -\eta_0 H_z(\bar{\rho}') \right. \\ \left. \times H_0^{(1)}(k_0 |\bar{\rho} - \bar{\rho}'|) - i \frac{(x - x')}{|\bar{\rho} - \bar{\rho}'|} \right. \\ \left. \times E_y(\bar{\rho}') H_1^{(1)}(k_0 |\bar{\rho} - \bar{\rho}'|) \right\} \Bigg|_{x'=a} \\ - \left[ -\eta_0 H_z(\bar{\rho}') H_0^{(1)}(k_0 |\bar{\rho} - \bar{\rho}'|) \right. \\ \left. - i \frac{(x - x')}{|\bar{\rho} - \bar{\rho}'|} E_y(\bar{\rho}') \right. \\ \left. \times H_1^{(1)}(k_0 |\bar{\rho} - \bar{\rho}'|) \right] \Bigg|_{x'=-a} \} \end{aligned} \quad (71)$$

where

$$\eta_0 = \sqrt{\frac{\mu_0}{\epsilon_0}} \quad (72)$$

$$\frac{\partial}{\partial \zeta} H_0^{(1)}(\zeta) = -H_1^{(1)}(\zeta) \quad (73)$$

$$H_m^{(1)}(\zeta) = J_m(\zeta) + iY_m(\zeta) \quad (74)$$

The zeroth- and first-order Bessel and Neumann functions are approximated by the following equations [14]:

$$J_0(\zeta) = \sum_{n=1}^7 a_0(n) \left( \frac{\zeta}{3} \right)^{2(n-1)} \quad (75)$$

$$\text{for } -3 \leq \zeta \leq 3$$

$$\begin{aligned} Y_0(\zeta) = \frac{2}{\pi} \ln \left( \frac{1}{2} \zeta \right) J_0(\zeta) \\ + \sum_{n=1}^7 b_0(n) \left( \frac{\zeta}{3} \right)^{2(n-1)} \end{aligned} \quad (76)$$

$$\text{for } 0 < \zeta \leq 3$$

where:

$$a_0(1) = 1.0, \quad a_0(2) = -2.2499997,$$

$$a_0(3) = 1.2656208, \quad a_0(4) = -0.3163866,$$

$$a_0(5) = 0.0444479, \quad a_0(6) = -0.0039444,$$

$$a_0(7) = 0.0002100$$

$$b_0(1) = 0.36746691, \quad b_0(2) = 0.60559366,$$

$$b_0(3) = -0.743200384,$$

$$b_0(4) = 0.25300117, \quad b_0(5) = -0.04261214,$$

$$b_0(6) = 0.00427916,$$

$$b_0(7) = -0.00024846$$

$$J_0(\zeta) = \zeta^{-1/2} \left[ \sum_{m=1}^7 f_0(m) \left(\frac{3}{\zeta}\right)^{m-1} \right] \\ \times \cos \left[ \zeta + \sum_{n=1}^7 \theta_0(n) \left(\frac{3}{\zeta}\right)^{n-1} \right] \quad (77) \\ \text{for } 3 \leq \zeta < \infty$$

$$Y_0(\zeta) = \zeta^{-1/2} \left[ \sum_{m=1}^7 f_0(m) \left(\frac{3}{\zeta}\right)^{m-1} \right] \\ \times \sin \left[ \zeta + \sum_{n=1}^7 \theta_0(n) \left(\frac{3}{\zeta}\right)^{n-1} \right] \quad (78) \\ \text{for } 3 \leq \zeta < \infty$$

$$f_0(1) = 0.79788456, \quad f_0(2) = -0.00000077,$$

$$f_0(3) = -0.00552740,$$

$$f_0(4) = -0.00009512, \quad f_0(5) = 0.00137237,$$

$$f_0(6) = -0.00072805, \quad f_0(7) = 0.00014476$$

$$\theta_0(1) = -0.78539816, \quad \theta_0(2) = -0.04166397,$$

$$\theta_0(3) = -0.00003954,$$

$$\theta_0(4) = 0.00262572, \quad \theta_0(5) = -0.00054125,$$

$$\theta_0(6) = -0.00029333, \quad \theta_0(7) = 0.00013558$$

$$J_1(\zeta) = \zeta \sum_{n=1}^7 a_1(n) \left(\frac{\zeta}{3}\right)^{2(n-1)} \quad (79) \\ \text{for } -3 \leq \zeta \leq 3$$

$$Y_1(\zeta) = \frac{2}{\pi} \ln \left( \frac{1}{2} \zeta \right) J_1(\zeta) \\ + \frac{1}{\zeta} \sum_{n=1}^7 b_1(n) \left(\frac{\zeta}{3}\right)^{2(n-1)} \quad (80) \\ \text{for } 0 < \zeta \leq 3$$

$$a_1(1) = 0.5, \quad a_1(2) = -0.56249985,$$

$$a_1(3) = 0.21093573, \quad a_1(4) = -0.03954289,$$

$$a_1(5) = 0.00443319, \quad a_1(6) = -0.00031761,$$

$$a_1(7) = 0.00001109$$

$$b_1(1) = -0.6366198, \quad b_1(2) = 0.2212091,$$

$$b_1(3) = 2.1682709,$$

$$b_1(4) = -1.3164827, \quad b_1(5) = 0.3123951,$$

$$b_1(6) = -0.0400976, \quad b_1(7) = 0.0027873$$

$$J_1(\zeta) = \zeta^{-1/2} \left[ \sum_{m=1}^7 f_1(m) \left(\frac{3}{\zeta}\right)^{m-1} \right] \\ \times \cos \left[ \zeta + \sum_{n=1}^7 \theta_1(n) \left(\frac{3}{\zeta}\right)^{n-1} \right] \quad (81) \\ \text{for } 3 \leq \zeta < \infty$$

$$Y_1(\zeta) = \zeta^{-1/2} \left[ \sum_{m=1}^7 f_1(m) \left(\frac{3}{\zeta}\right)^{m-1} \right] \\ \times \sin \left[ \zeta + \sum_{n=1}^7 \theta_1(n) \left(\frac{3}{\zeta}\right)^{n-1} \right] \quad (82) \\ \text{for } 3 \leq \zeta < \infty$$

$$f_1(1) = 0.79788456, \quad f_1(2) = 0.00000156,$$

$$f_1(3) = 0.01659667,$$

$$f_1(4) = 0.00017105, \quad f_1(5) = -0.00249511,$$

$$f_1(6) = 0.00113653, \quad f_1(7) = -0.00020033$$

$$\theta_1(1) = -2.35619449, \quad \theta_1(2) = 0.12499612,$$

$$\theta_1(3) = 0.00005650,$$

$$\theta_1(4) = -0.00637879, \quad \theta_1(5) = 0.00074348,$$

$$\theta_1(6) = 0.00079824, \quad \theta_1(7) = -0.00029166$$

In the finite difference-time domain scheme, it is relatively simple to obtain the fields over a closed surface. For a finite geometry, the scattered fields can be sampled on a rectangular box which encloses the entire geometry (Figure 6). For an infinite ground plane geometry, the scattered fields are sampled on three sides of a box which encloses any discontinuities in or above the infinite ground plane (Figure 7). Image theory allows the replacement of the infinite ground plane with image sources. The appropriate image fields are shown for infinite perfect electric and magnetic conducting planes in Figure 9. From Figure 9, it is apparent that the tangential fields have been obtained on a closed surface. Note that the field solution obtained using the image sources is not valid in the image half space.

Sinusoidal and Gaussian pulse time-dependent excitations are treated differently in order to obtain the necessary time harmonic complex amplitudes of the fields on a closed surface. For sinusoidal time dependent excitations, it is relatively simple to ob-

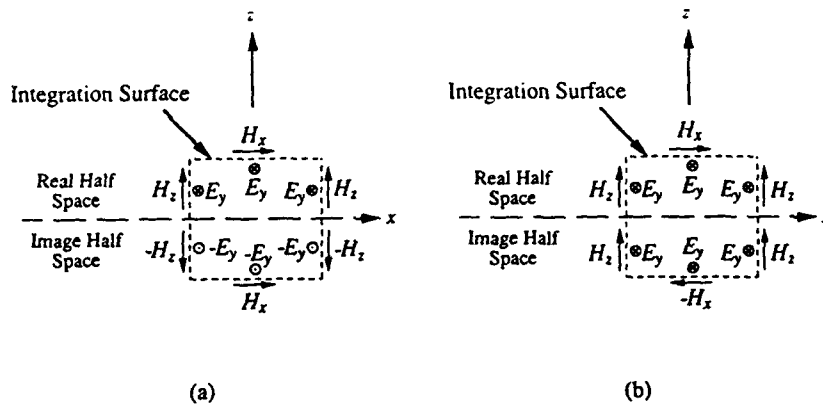


Figure 9 Image Sources for the  $E$ -Field Polarization With an Infinite Ground Plane. (a) Electric Conductor. (b) Magnetic Conductor.

tain the complex amplitudes of the fields by sampling the fields after steady state has been reached. The amplitudes can be obtained by recording the maximum values of the fields. The relative phases can be obtained by recording and comparing the time of the maximum values of the fields. For Gaussian pulse time-dependent excitations, Fourier transformation of the excitation source and the fields is performed. At a particular frequency, by dividing the complex Fourier amplitudes of the fields by the Fourier amplitude of the excitation, the complex amplitudes of the fields can be obtained for an excitation source with unity amplitude. For sinusoidal time-dependent excitations, fields and, hence, radiation patterns can only be obtained for a single frequency. However, for Gaussian pulse time-dependent excitations, fields and radiation patterns can be obtained for multiple frequencies. Some limitations to the range of frequencies that can be analyzed are that the grid must be fine enough to adequately model the frequency of interest and that the Gaussian pulse must contain a significant amount of energy at that frequency.

#### 4. NUMERICAL RESULTS AND DISCUSSION

Various electromagnetic phenomena were examined and animated utilizing the FD-TD code. A few of the electromagnetic phenomena which are examined using this code include: leading and trailing edge diffractions from a conducting strip and their dependence on polarization, creeping waves around a conducting cylinder, slit diffraction with plane-wave excitation, propagation through dielectric and lossy media, excitation of a waveguide by a line

source, and interaction of multiple line current sources. In each of the surface plots, shown in Figures 10–16, the outlines of the scatterers and the line sources will be represented by a uniform small positive height. The size of the computational domain used to perform these simulations was 200 nodes  $\times$  200 nodes. The physical size of the computational domain was chosen to be 10 meters  $\times$  10 meters. Hence,  $\Delta x = 0.05$  m and  $\Delta z = 0.05$  m.

The scatterer in the first two cases is a thin perfect electric conducting strip which is in the center of the computational domain. The strip is 3.5 meters wide and 0.1 meters thick. The excitation source is a Gaussian pulse plane wave which is incident at 7 degrees above the plane of the strip. The pulse width is 0.354 meters and is defined to be equal to two standard deviations of the Gaussian pulse. The shape

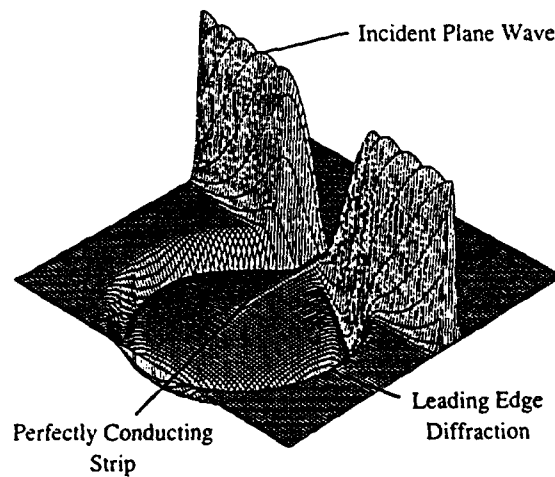


Figure 10 Leading Edge Diffraction from a Perfectly Conducting Strip for  $E$ -Field Polarization.

of the Gaussian pulse is given by the following equation

$$f(x) = e^{-x^2/(2\lambda_0^2)} \quad (84)$$

where  $x_0 = 0.177$  m. The first case involves the  $E$ -field polarization and is illustrated in Figure 10. For Figure 10, the electric field,  $E_y$ , which is in the uniform and infinite direction, is plotted. The Gaussian pulse plane wave appears as a fairly uniform hill which stretches across the entire computational domain. The pulse is moving from left to right on the figure. The surface plot was recorded when the Gaussian pulse plane wave had already propagated near the end of the strip. The ring, which is centered at one edge of the strip, is the leading edge diffraction from the edge of the strip which was illuminated first by the plane wave. The diffraction from the leading edge, in this case, is strong because there is a strong discontinuity in the electric field when the pulse is incident on the leading edge. The perfect electric conductor requires the tangential electric field at the surface to be zero. Hence, when the incident electric field, which is parallel to the strip surface, impinges on the strip, a strong reflected wave is generated in order to satisfy the boundary conditions. At the trailing edge, the boundary condition states that the current must be continuous. The surface current,  $K$ , is defined to be

$$\vec{K} = \hat{n} \times \vec{H} \quad (85)$$

Since the magnetic field is almost perpendicular to the strip, the tangential magnetic fields at the surface will be weak. Thus, the surface currents will also be

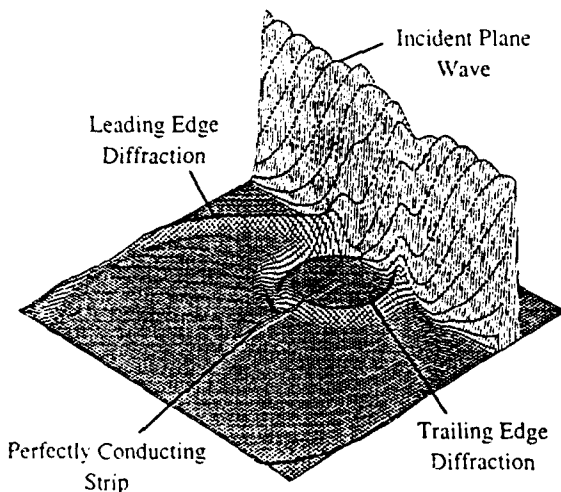


Figure 11 Trailing Edge Diffraction From a Perfectly Conducting Strip for  $H$ -Field Polarization.

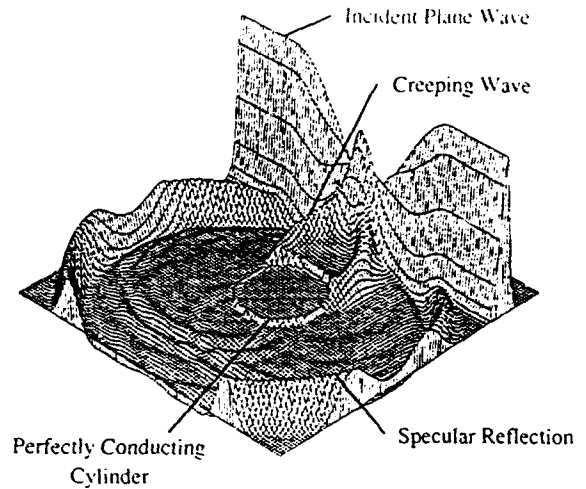


Figure 12 Creeping Waves Around a Perfectly Conducting Cylinder for  $H$ -Field Polarization.

weak, and there will be little diffraction at the trailing edge. The second case, which is illustrated in Figure 11, involves the  $H$ -field polarization. In this case, the magnetic field,  $H_x$ , is plotted. The Gaussian pulse plane wave has propagated past the strip, and now two circular rings can be seen. The larger ring is the leading edge diffraction, which is weaker than the previous case because the electric field of the incident plane wave points nearly perpendicularly to the strip, and causes a less severe discontinuity in the tangential electric field at the strip surface. The smaller ring represents the trailing edge diffraction. In this case, the surface currents will be particularly strong, because the magnetic field is always parallel to the strip's surface. The strong trailing edge diffraction is due to the large discontinuity in the surface current at the trailing edge of the strip.

The third scatterer involves a perfectly conducting cylinder. The excitation source is again a Gaussian pulse plane wave which is incident at 90 degrees for the  $H$ -field polarization. The cylinder has a diameter of 2.5 meters, and the pulse width is again 0.354 meters. Figure 12 illustrates the magnetic field,  $H_x$ , as the plane wave scatters off the cylinder. Again, the incident plane wave can be seen after it has propagated past the cylinder. The circular arc is traveling outward away from the cylinder and is the specular reflection from the cylinder. In the vicinity of the shadow region, where the cylinder blocks the incident plane wave, the circular arc is still attached to the conducting cylinder and travels around the back of the cylinder. This phenomenon corresponds to a creeping wave. Creeping waves occur much more strongly for the  $H$ -field polarization, because

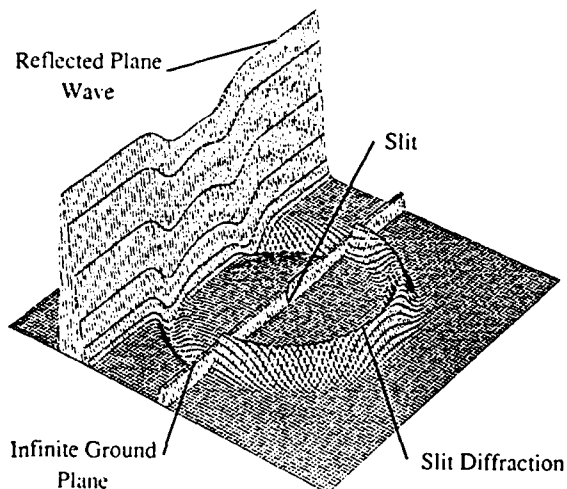


Figure 13 Diffraction of a Plane Wave Through a Slit in an Infinite Perfectly Conducting Ground Plane for  $H$ -Field Polarization.

stronger surface currents are generated, which essentially allow the fields to remain attached to the cylinder.

The fourth case illustrates diffraction of a plane wave through a slit in an infinite perfect electric conducting ground plane. The infinite ground plane is 0.1 meters thick and the slit is 0.3 meters wide. The plane wave is normally incident upon the ground plane from the upper half space and has a Gaussian pulse time dependence with a pulse width of 0.4 meters. In this case, the  $H$ -field polarization is examined, and Figure 13 shows the magnetic field,  $H_y$ . The reflected plane wave is evident and has only been slightly perturbed by the presence of the slit. The fields that pass through the slit radiate cylindrically from the aperture, thus illustrating slit diffraction.

Figure 14 illustrates the propagation of a Gaussian pulse plane wave through a dielectric cylinder for the  $H$ -field polarization. The cylinder has a diameter of 2.5 meters, and the pulse width is again 0.354 meters. The dielectric cylinder has  $\epsilon_r = 2$ ,  $\mu_r = 1$ , and  $\sigma = \sigma_m = 0$ . Figure 14 shows the magnetic field,  $H_y$ . The specular reflection off the cylinder is not as strong as the specular reflection for the perfectly conducting cylinder because some of the fields are reflected and some are transmitted. The fields within the dielectric cylinder lag behind the fields in free space because they propagate at a slower velocity in the dielectric than in free space. The magnetic fields within the cylinder have higher intensities for the following reasons. First, the phase matching condition on the surface of the dielectric cylinder

tends to bend the electromagnetic waves toward the bisector of the cylinder which is parallel to the incident wave vector, which focuses the fields to some extent. The reflection coefficient at a planar boundary between free space and a dielectric with relative permittivity greater than 1 for the  $H$ -field polarization is always greater than zero. Hence, the transmission coefficient will always be greater than 1, and the magnetic fields transmitted through the dielectric will be greater than the incident magnetic fields. Treating each point of the dielectric cylinder locally as a planar interface, it is clear that the magnetic fields within the cylinder will be greater than the incident fields outside the cylinder.

The next case examines the excitation of the perfectly conducting parallel plate waveguide by a line current source. The waveguide is 0.55 meters tall and assumed to be infinite in length, and the thickness of the walls is 0.1 meters. The line source is vertically centered within the cavity and is located in the middle of the section of the waveguide shown. The  $H$ -field polarization is examined and magnetic field,  $H_y$ , is plotted in Figure 15. The line current source radiates at a frequency of 200 MHz. The wavelength in free space is 1.5 meters. The line current source excites the TEM mode within the waveguide. Two waves, which travel in opposite directions, are launched by the line source. There is also a lossy dielectric material which spans the height of the waveguide and is 0.9 meters wide. The lossy material has  $\epsilon_r = \mu_r = 1$ ,  $\sigma = 0.1$ , and  $\sigma_m = 0$ . The fields are attenuated as they propagate through the dielectric and it is apparent that the fields that have passed through lossy dielectric are smaller than the fields which have not.

The last case illustrates the interference pattern generated by four line sources. Figure 16 plots the

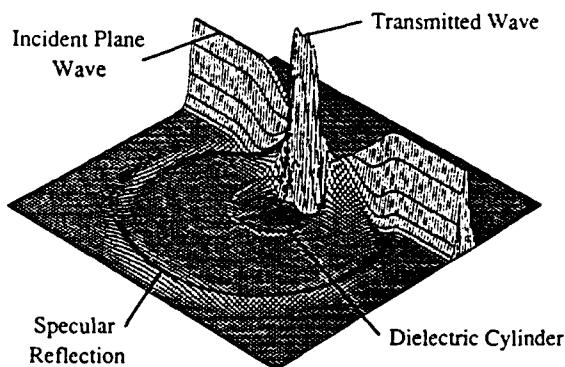


Figure 14 Propagation Through a Dielectric Cylinder With  $\epsilon_r = 2$ ,  $\mu_r = 1$ , and  $\sigma = \sigma_m = 0$  for  $H$ -Field Polarization.

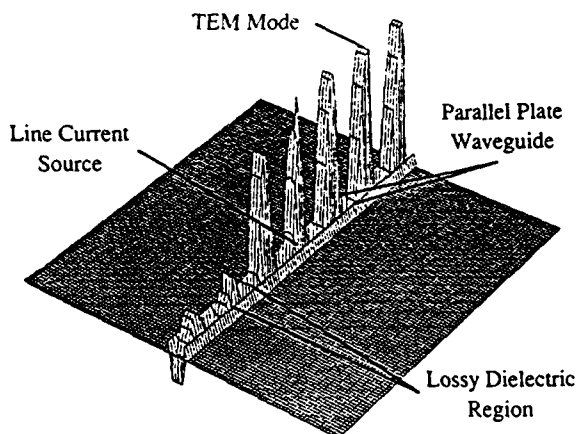


Figure 15 Excitation of a Parallel Plate Waveguide by a Line Current Source, and Propagation Through a Lossy Dielectric With  $\epsilon_r = \mu_r = 1$ ,  $\sigma = 0.1$ , and  $\sigma_m = 0$  for  $H$ -Field Polarization.

electric field,  $E_y$ , for the  $E$ -field polarization. The line sources are excited at a frequency of 333.3 MHz. In free space, the wavelength is 0.9 meters. The line current sources are separated by 0.45 meters, or half a wavelength. The line sources are in phase and have equal magnitudes or, in other words, have the exact same time dependence. On the line on which the line sources lie, the radiation is very small since the radiation from each line source almost exactly cancels the radiation from the adjacent line sources. On this line, the radiation from each line source will be  $180^\circ$  out of phase with the next line source, because they are each spatially separated by half a wavelength in this direction. On the line perpendicular to the line connecting the four line sources, the radiation from the line sources will add constructively. The waves reinforce each other because they are in phase since every point on this line is almost equidistant to the four line sources. Hence, the radiation will

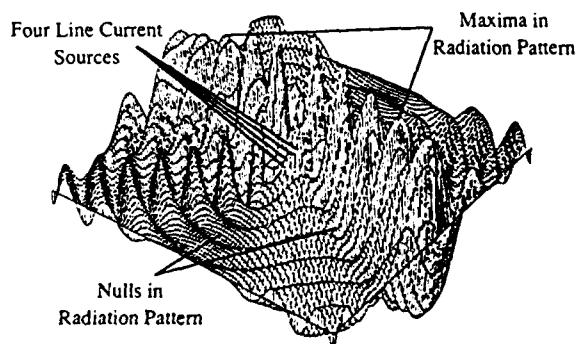


Figure 16 Interference Pattern Produced by Four Line Sources for  $E$ -Field Polarization.

be largest in these two directions. There will also be additional nulls and maxima as the four line sources add constructively and destructively for different directions.

Due to the limitations of the surface plots and the inability to include color plots, it was not possible to show all the capabilities of the code in this study. One extremely useful aspect of this code is the capability to calculate and successively display the fields in color in order to visually produce the propagation of electromagnetic waves in real time. The typical computational time for animation consisting of 500 time steps and 100 color plots is less than 1 hour on a 33-MHz IBM 386 compatible personal computer. After the FD-TD computation has been completed, the actual animation can be played back at about five frames per second.

In addition to the capability to visualize the fields, the computer code can generate radiation and scattering patterns. Figures 17–20 illustrate radiation from a linear array, and scattering from a perfectly conducting strip and a large slit in an infinite ground plane. In each of these polar plots, the field amplitude is represented in dB for a radius of 50 meters. For  $E$ -field polarization cases,  $E_y$  is plotted, and a complex amplitude of 1 V/m is assumed for the excitation source. For  $H$ -field polarization cases,  $H_y$  is plotted, and a complex amplitude of 1 A/m is assumed for the excitation source.

The radiation pattern of the four-element array previously examined in Figure 16 is illustrated in Figure 17. Four line current sources for the  $E$ -field polarization are excited at a frequency of 333.3

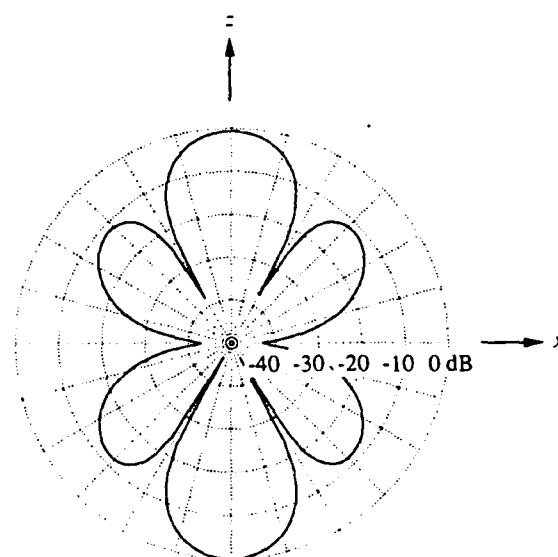


Figure 17 Radiation Pattern of a Four-Element Array of Line Sources for  $E$ -Field Polarization

MHz, and the sources are separated by 0.45 meters or half a wavelength. The line sources have the same phase and magnitude. The radiation pattern has four-fold symmetry since the problem has four-fold symmetry. The radiation pattern has nulls in the  $+x$ ,  $-x$  directions,  $60^\circ$  and  $120^\circ$  above and below the  $x$ -axis. The main lobes are in the  $+z$  and  $-z$  directions. The main lobes correspond to a electric field of  $0.3096 \text{ V/m}$ . Recall that the line sources are uncalibrated, so that the absolute numbers will be dependent on the grid size. The radiation pattern obtained here is consistent with the radiation pattern that would be obtained using linear array theory.

Figure 18 shows the scattering pattern of perfect electric conducting strip. The strip is illuminated by a 300-MHz sinusoidal plane wave at an angle of  $45^\circ$  above the  $x$ -axis for the  $E$ -field polarization. The dimensions of the strip are  $3.1 \text{ m} \times 0.1 \text{ m}$ . As expected, the main lobes of the scattering pattern occur in the specular direction ( $135^\circ$  above the  $x$ -axis) and the forward scatter direction ( $135^\circ$  below the  $x$ -axis). The maximum scattered electric field is  $0.268 \text{ V/m}$ .

Figures 19 and 20 show the radiation patterns for a large slit illuminated by a Gaussian pulse plane wave at normal incidence from the lower half space for the  $H$ -field polarization. The slit is  $4.9 \text{ m}$  wide and the infinite perfect electric conducting plane is  $0.1 \text{ m}$  thick. Since a Gaussian pulse time dependence is used, multiple frequencies can be analyzed. The frequencies examined in Figures 19 and 20 are 300 MHz and 400 MHz, respectively, and the corre-

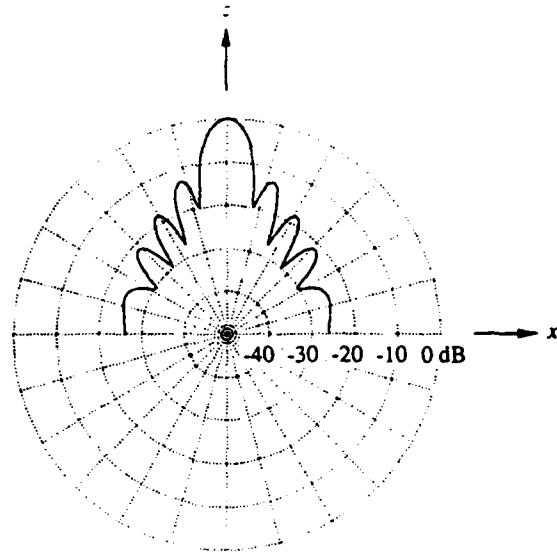


Figure 19 Diffraction Pattern of a Slit in an Infinite Ground Plane Illuminated at Normal Incidence at 300 MHz for  $H$ -Field Polarization.

sponding wavelengths are  $1 \text{ m}$  and  $0.75 \text{ m}$ . The maximum peaks in the radiation pattern occur in  $+z$  direction and are  $0.650 \text{ A/m}$  at 300 MHz and  $0.809 \text{ A/m}$  at 400 MHz. Fraunhofer diffraction states that the fields in an aperture are related to the far-field pattern by a Fourier transform [13]. In these cases, the field distribution is essentially uniform over the aperture, so the far-field patterns should have a  $\frac{\sin x}{x}$  dependence. At the higher frequency,

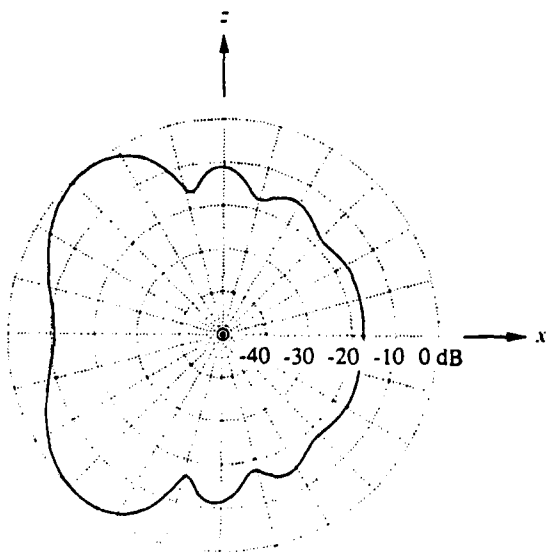


Figure 18 Scattering Pattern of a Perfectly Conducting Strip Illuminated at a  $45^\circ$  Grazing Angle for  $E$ -Field Polarization.

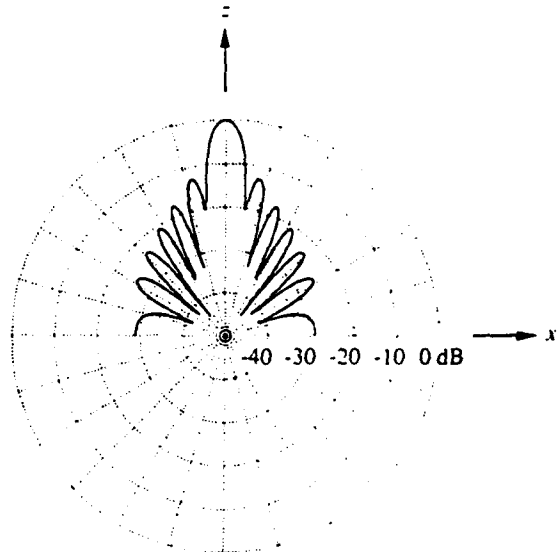


Figure 20 Diffraction Pattern of a Slit in an Infinite Ground Plane Illuminated at Normal Incidence at 400 MHz for  $H$ -Field Polarization.

the aperture is electrically larger, so its transform, and hence, radiation pattern, is a narrower sinc function.

## 5. SUMMARY

This FD-TD code can be used to examine various electromagnetic phenomena. The code successfully and accurately predicted the interaction between various sources and objects. Because the FD-TD technique has the capability to animate propagation, diffraction and scattering of electromagnetic waves, it is well suited as an educational tool for students of electromagnetic wave theory and its applications. The additional capability of generating radiation patterns provides an alternative, more quantitative way of viewing electromagnetic radiation.

## ACKNOWLEDGMENTS

This work was supported by a Digital Equipment Corporation Contract, an ONR Grant N00014-90-J-1002, the Joint Service Electronics Program under the Contract DAAL03-89-C-001, and a U.S. Air Force Laboratory Graduate Fellowship.

## REFERENCES

- [1] K. S. Yee, "Numerical solution of initial boundary value problems involving Maxwell's equations in isotropic media," *IEEE Trans. Ant. Propagat.*, Vol. AP-14, pp. 302-307, 1966.
- [2] K. Li, "Electromagnetic wave scattering by surface discontinuities in a perfectly conducting ground plane," *Master's Thesis*, Department of Electrical Engineering and Computer Science, M.I.T., Cambridge, MA, 1990.
- [3] A. Taflov and M. E. Brodwin, "Numerical solution of steady-state electromagnetic scattering problems using the time-dependent Maxwell's equations," *IEEE Trans. Microwave Theory Tech.*, Vol. MTT-23, pp. 623-630, 1975.
- [4] C. F. Lee, R. T. Shin, J. A. Kong, and B. J. McCartin, "Finite difference-time domain techniques on triangular grids," *Progress in Electromagnetics Research Symposium*, Boston, MA, July 25-26, 1989.
- [5] M. A. Morgan (Ed.), *PIER 2: Finite Element and Finite Difference Methods in Electromagnetic Scattering*. Elsevier, New York, 1990.
- [6] A. Bayliss, C. I. Goldstein, and E. Turkel, "On accuracy conditions for the numerical computation of waves," *J. Comp. Phys.*, Vol. 59, pp. 396-404, 1985.
- [7] M. Moghaddam, W. C. Chew, B. Anderson, E. Yanakakis, and Q. H. Liu, "Computation of transient electromagnetic waves in inhomogeneous media," *Radio Sci.*, Vol. 26, pp. 265-273, 1991.
- [8] C. F. Lee, "Finite difference method for electromagnetic scattering problems," Ph.D. Thesis, Department of Electrical Engineering and Computer Science, M.I.T., Cambridge, MA, 1990.
- [9] B. Engquist and A. Majda, "Absorbing boundary conditions for the numerical simulation of waves," *Math. Comp.*, Vol. 31, pp. 629-651, 1977.
- [10] G. Mur, "Absorbing boundary conditions for the finite-difference approximation of the time-domain electromagnetic-field equations," *IEEE Trans. Electromagn. Compat.*, Vol. EMC-23, pp. 377-382, 1981.
- [11] A. Bayliss and E. Turkel, "Radiation boundary conditions for wave-like equations," *Comm. Pure Appl. Math.*, Vol. 33, pp. 707-725, 1980.
- [12] L. N. Trefethen and L. Halpern, "Well-posedness of one-way equations and absorbing boundary conditions," *NASA Contractor Report No. 172619*. Institute for Computer Applications in Science and Engineering, NASA Langley Research Center, Hampton, VA, 1985.
- [13] J. A. Kong, *Electromagnetic Wave Theory*. Wiley, New York, 1986.
- [14] M. Abramowitz and I. A. Stegun, *Handbook of Mathematical Functions with Formulas, Graphs, and Mathematical Tables*. National Bureau of Standards, Department of Commerce, Washington DC.

## BIOGRAPHIES



Kevin Li received his BS and SM degrees (1990) in Electrical Engineering and EE (Electrical Engineer's degree (1991) from the Massachusetts Institute of Technology, where he is currently pursuing his PhD in Electrical Engineering. Since 1990, he has been the recipient of a United States Air Force Laboratory Graduate Fellowship. His main research interests include electromagnetic scattering, radar cross section prediction, and numerical techniques. Mr. Li is a member of Tau Beta Pi and a student member of IEEE.



M. Ali Tassoudji received his BS (1987) and MS (1989) degrees in Electrical Engineering from the University of Michigan, Ann Arbor. Since 1989, he has been a research assistant at the Massachusetts Institute of Technology, where he is currently working towards his PhD in Electrical Engineering. His research interests include electromagnetic scattering and propagation, modeling of microwave circuits, and numerical techniques. Mr. Tassoudji is a member of IEEE and Eta Kappa Nu.



Robert T. Shin received his SB (1977), SM (1980), and PhD (1984) in Electrical Engineering from the Massachusetts Institute of Technology. Since 1984 he has been a member of the Air Defense Techniques Group at MIT Lincoln Laboratory, as a Research Staff member and as a Senior Staff member from 1989. His research interests are in the areas of electromagnetic wave scattering and propagation, theoretical model development, and data interpretation for microwave remote sensing. He is the coauthor of *Theory of Microwave Remote Sensing* (Wiley, 1985). Dr. Shin is a member of The Electromagnetics Academy, IEEE, American Geophysical Union, Tau Beta Pi, Eta Kappa Nu, and Commission F of the International Union of Radio Science. Since 1987 he has served on the Editorial Board of the *Journal of Electromagnetic Waves and Applications* (JEWA).



Jin Au Kong is Professor of Electrical Engineering and Chairman of Area IV on Energy and Electromagnetic Systems in the Department of Electrical Engineering and Computer Science at the Massachusetts Institute of Technology in Cambridge, Massachusetts. In 1977-80 he served the United Nations as a High-Level Consultant to the Under-Secretary-General on science and technology, and as an Interregional Advisor on remote sensing technology for the Department of Technical Cooperation for Development. His research interest is in the area of electromagnetic wave theory and applications.

## Time Domain Modeling of Impedance Boundary Condition

C. F. Lee, R. T. Shin, and J. A. Kong

**Abstract**—A methodology developed to handle dispersive materials in the time domain is extended to model the dispersive characteristics of the impedance boundary condition used for a thin layer coating over perfect conductors. The impedance boundary condition is first approximated as a rational function of frequency. This rational function is then transformed to a time domain equation, resulting in a partial differential equation in space and time. Discretization of the time domain model to efficiently handle the thin layer coating is presented in the context of the finite-difference time-domain (FD-TD) technique. The methodology is verified by solving a one-dimensional problem using the FD-TD technique and comparing with the analytical results.

### I. INTRODUCTION

Electrically fine structures often appear in practical applications. To resolve the electromagnetic behavior of these structures, very fine grids are needed in numerical techniques (e.g., the finite-difference time-domain technique). Alternatively, one may incorporate the localized physical behavior, such as the impedance boundary condition [1] and thin wire formulations [2], [3], of these fine structures into discretization schemes.

Thin surface coatings on metallic bodies appear in many scattering problems. In principle, these thin surface coatings can be modeled numerically and geometrically by very fine grids with appropriate discretization schemes. The disadvantage associated with such an approach is the large computer memory requirement. Furthermore, in the finite-difference time-domain (FD-TD) technique, the time increment is usually determined by the smallest grid size in the entire computational domain to satisfy the stability condition.

In modeling a thin layer coating in the frequency domain, the concept of impedance boundary condition can be used to avoid the fine layers of grids. The impedance boundary condition relates the tangential fields on the coating to their normal derivatives, which is derived using the configuration of a half-space conductor with thin layer coating. The resulting impedance boundary condition is frequency dependent, and this dispersive nature of the impedance boundary condition causes difficulty in the time domain modeling. In this paper, a time domain technique used to treat dispersive materials is employed to convert the impedance boundary condition to the time domain [4]. Following the idea in [5], the impedance boundary condition is approximated by a rational function of the frequency. Then, the tangential fields are related to their normal derivatives by a partial differential equation in space and time. A numerical discretization scheme in the context of the FD-TD tech-

nique is discussed and the overall scheme is verified numerically for a one-dimensional configuration.

### II. TIME DOMAIN DESCRIPTION OF THE IMPEDANCE BOUNDARY CONDITION

The impedance boundary condition of the coated conductor can be derived based on a two-layer configuration (Fig. 1). By ignoring the variation along the tangential directions, the tangential electric field can be related to its normal derivative by the following equation:

$$E = \frac{\eta_r}{k} \tan(k \Delta \sqrt{\mu_r \epsilon_r}) \frac{\partial E}{\partial y}, \quad (1)$$

where  $k$  is the free space wavenumber,  $\mu_r$  and  $\epsilon_r$  are the relative permeability and relative permittivity, respectively, and  $\eta_r = \sqrt{\mu_r/\epsilon_r}$  is the relative impedance (impedance normalized to  $\eta_0$ ). Inverse Fourier transformation may be used to convert the above equation to the time domain. However, it is relatively complicated and the result may not be suitable for numerical analysis. Instead, following the procedure outlined in [5], the above equation is approximated using a rational function of the frequency. With the substitution of  $-i\omega$  by  $\partial/\partial t$ , the time domain description of the impedance boundary condition is obtained.

The rational function approximated of (1) can be obtained by expressing the *tangent* function as the ratio of *sine* and *cosine*. Next, the Taylor series expansions of these two functions are used to obtain the rational function form. By keeping the first two terms in the Taylor series expansions of the *sine* and *cosine* functions, the first-order rational function approximation is obtained.

$$E = \eta_r \Delta \sqrt{\mu_r \epsilon_r} \frac{1 - \frac{1}{6} k^2 \Delta^2 \mu_r \epsilon_r}{1 - \frac{1}{2} k^2 \Delta^2 \mu_r \epsilon_r} \frac{\partial E}{\partial y}. \quad (2)$$

Similarly, by keeping the first three terms of Taylor series expansion, the second-order approximation can be obtained:

$$E = \eta_r \Delta \sqrt{\mu_r \epsilon_r} \frac{1 - \frac{1}{6} k^2 \Delta^2 \mu_r \epsilon_r + \frac{1}{120} k^4 \Delta^4 \mu_r^2 \epsilon_r^2}{1 - \frac{1}{2} k^2 \Delta^2 \mu_r \epsilon_r + \frac{1}{24} k^4 \Delta^4 \mu_r^2 \epsilon_r^2} \frac{\partial E}{\partial y}. \quad (3)$$

In general, both the relative permittivity and permeability in (2) and (3) can be complex to account for electric and magnetic losses. However, in this paper, we will consider only the loss due to electrical conductivity.

The time domain expressions corresponding to (2) and (3) can be obtained by substituting  $-i\omega$  by  $\partial/\partial t$ , or equivalently,  $-ik$  by  $\partial/\partial \tau$ , where  $\tau = c_0 t$  is the normalized time. Assuming electrical conduction loss only, we obtain

$$\epsilon_r = \epsilon' + i \frac{\sigma \eta_0}{k}, \quad (4)$$

where  $\epsilon'$ ,  $\sigma$  and  $\eta_0$  are dielectric constant, electric conductivity and free space impedance, respectively. The first-order time domain description of the impedance boundary condition corresponding to

Manuscript received September 9, 1991; revised February 10, 1992. This work was supported in part by ONR Contract N00014-90-J-1002 and the Joint Services Electronics Program under the Contract DAAL03-89-C-0001.

C. F. Lee is with WaveTracer, Inc., Acton, MA 01720.

R. T. Shin and J. A. Kong are with the Department of Electrical and Engineering and Computer Science, and Research Laboratory of Electronics, Massachusetts Institute of Technology, Cambridge, MA 02139.

IEEE Log Number 9201728.

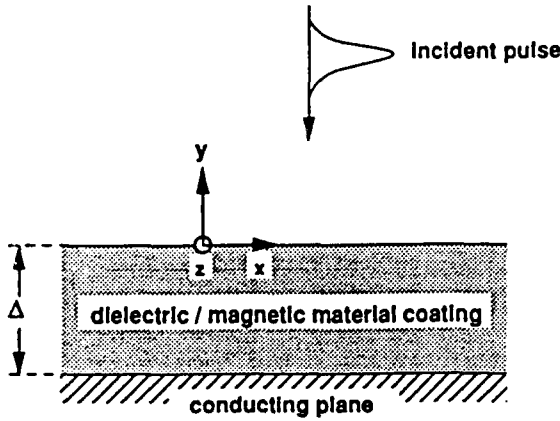


Fig. 1. Two-layer configuration.

(2) is given by

$$\begin{aligned} & \left[ 1 + \frac{1}{2} \mu_r \Delta^2 \sigma \eta_0 \frac{\partial}{\partial \tau} + \frac{1}{2} \Delta^2 \epsilon' \mu_r \frac{\partial^2}{\partial \tau^2} \right] E \\ & = \Delta \left[ 1 + \frac{1}{6} \mu_r \Delta^2 \sigma \eta_0 \frac{\partial}{\partial \tau} + \frac{1}{6} \Delta^2 \epsilon' \mu_r \frac{\partial^2}{\partial \tau^2} \right] \frac{\partial E}{\partial y} \end{aligned} \quad (5)$$

Applying the same transformation to (3), the second-order time domain description of the impedance boundary condition is given by

$$\begin{aligned} & \left[ 1 + \frac{1}{2} \Delta^2 \sigma \eta_0 \frac{\partial}{\partial \tau} + \left( \frac{1}{2} \Delta^2 \epsilon' + \frac{1}{24} \Delta^4 \sigma^2 \eta_0^2 \right) \frac{\partial^2}{\partial \tau^2} \right. \\ & \quad \left. + \frac{1}{12} \Delta^4 \epsilon' \sigma \eta_0 \frac{\partial^3}{\partial \tau^3} + \frac{1}{24} \Delta^2 \epsilon'^2 \frac{\partial^4}{\partial \tau^4} \right] E \\ & = \Delta \left[ 1 + \frac{1}{6} \Delta^2 \sigma \eta_0 \frac{\partial}{\partial \tau} + \left( \frac{1}{6} \Delta^2 \epsilon' + \frac{1}{120} \Delta^4 \sigma^2 \eta_0^2 \right) \frac{\partial^2}{\partial \tau^2} \right. \\ & \quad \left. + \frac{1}{60} \Delta^4 \epsilon' \sigma \eta_0 \frac{\partial^3}{\partial \tau^3} + \frac{1}{120} \Delta^2 \epsilon'^2 \frac{\partial^4}{\partial \tau^4} \right] \frac{\partial E}{\partial y} \end{aligned} \quad (6)$$

The above time domain descriptions of the impedance boundary condition are partial differential equations in space and time. In fact, these equations may be derived directly in the time domain with a finite difference approximation and a simple averaging scheme [4] (see Appendix). The impedance boundary condition accounts for the interaction between air-dielectric interface and conducting surface. In the time domain there is a time delay associated with this interaction. This delay is partially modeled by (5) and (6).

### III. DISCRETIZATION

There are many discretization schemes one can use to discretize (5) and (6) for the finite-difference time-domain technique. The discretization of the normal derivative is quite important in the implementation of the impedance boundary condition. In order to have an accurate approximation, the vanishing tangential electric field on the conducting surface is used. This leads to interpolation of the electric field in three or more locations. Employing the Lagrange interpolation formula for three electric fields (Fig. 2), the normal derivative is discretized as follows:

$$\left. \frac{\partial E}{\partial y} \right|_1 = \frac{a}{\Delta_y (1+a)} \left[ E_2 \frac{a^2 - 1}{a^2} E_1 \right] \quad (7)$$

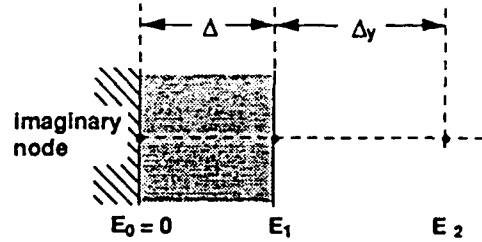


Fig. 2. Discretization nodes for normal derivative.

In the above equation  $a$  represents the ratio of the layer thickness to the grid size,  $\Delta/\Delta_y$ . It turns out that a better approximation of the normal derivative can be obtained by including the effect of the dielectric constant of the coating. Because the wave velocity in the coating is slower than that in the free space where discretization applied, the effective thickness of the coating should be  $\Delta\sqrt{\epsilon'}$ . Therefore, the following equation is used:

$$a = \frac{\Delta\sqrt{\epsilon'}}{\Delta_y}$$

The temporal derivatives in (5) and (6) may also be discretized in many forms. A simple second-order center-differencing is used in this paper.

### IV. NUMERICAL RESULTS

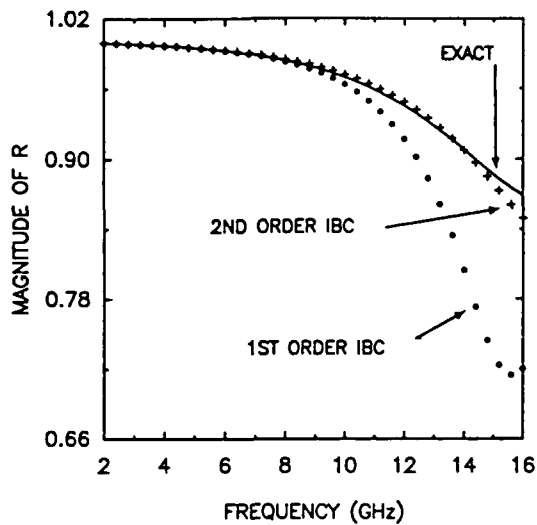
Equations (5) and (6) describe the time domain modeling of the impedance boundary condition given by (1). Equation (7) and center-differencing in time provide a possible discretization scheme. To validate the approach outlined in this paper, a one-dimensional reflection problem is simulated using these models together with the finite-difference time-domain method [3]. The reflected wave is calculated in the time domain and Fourier transformed to obtain the reflection coefficient as a function of frequency. The results are compared with the exact solution obtained directly in the frequency domain.

Fig. 1 shows the configuration of the problem. The layer has thickness of 0.2 cm. The coating material is assumed to have dielectric constant of 5 and conductivity of 0.2 mho/meter. The computation domain contains 500 nodes with grid size being 0.2 cm. The normalized time increment  $\Delta$ , is 0.2 cm to satisfy the stability criterion and to minimize numerical dispersion. At the first node of the computational domain, an incident Gaussian pulse modulated by a carrier at 8 GHz is imposed. This Gaussian pulse has a half-power pulse width of 0.0625 nano-second, which corresponds to a bandwidth of 6 GHz. The last node of the computational domain is placed at the free space/dielectric interface where the first-order or the second-order approximation to the impedance boundary condition (IBC) is applied to simulate the thin layer coating.

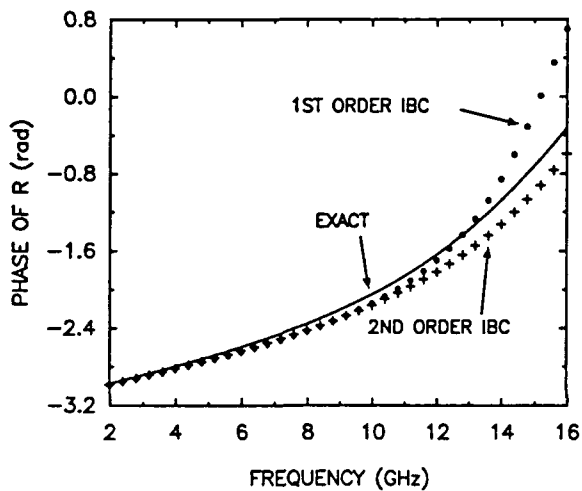
The exact solution for the reflection coefficient is given by

$$R(k) = \frac{i\eta_r \tan(k \Delta \sqrt{\mu_r \epsilon_r}) + 1}{i\eta_r \tan(k \Delta \sqrt{\mu_r \epsilon_r}) - 1} \quad (8)$$

where  $\eta_r$  and  $\epsilon_r$  is complex. For the assumed parameters, the magnitude and the phase of this reflection coefficient are plotted in Fig. 3(a) and (b) (solid curves), respectively, from 2 GHz to 16 GHz. The results obtained by using the FD-TD simulation are also shown in Fig. 3(a) and (b). The "○" and "+" curves represent results



(a)



(b)

Fig. 3. (a) Magnitude of reflection coefficient versus frequency. (b) Phase of reflection coefficient versus frequency.

obtained using (5) and (6), respectively. Both the first- and the second-order approximations yield good agreement with the exact solution in the phase of the reflection coefficient. However, the advantage of using the second-order approximation, (6), is clearly shown in the magnitude of the reflection coefficient. The results obtained using the first-order approximation match the exact solution at low frequencies with increasing discrepancy at higher frequencies.

Fig. 4 shows the percent error of the reflection coefficient magnitude as a function of the coating thickness. These errors are for the FD-TD results with the second-order approximation of the IBC using the same grid size and the same material parameters while varying the coating thickness. The three curves represent errors at three different frequencies. The errors for the half-power frequencies, 5 GHz and 11 GHz, are shown by " + " and " × " respectively. The errors at the carrier frequency are shown by " ○ ". These errors are all well within 1.0 percent, and they increase with increasing thickness, as expected. It should be noted that the errors are relatively small even when the thickness of the coating is up to 1/5 of the wavelength inside the layer as in the case of 11 GHz at the thickness of 0.25 cm.

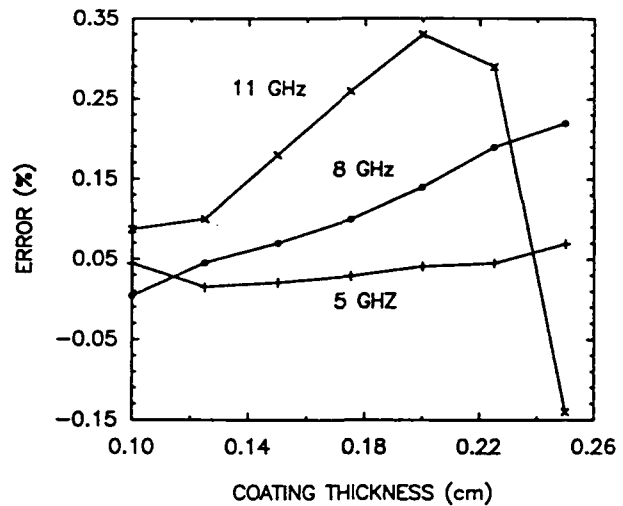


Fig. 4. Percentage error for second-order IBC versus coating thickness.

## V. SUMMARY

In this paper, a time domain modeling of the impedance boundary condition is derived and expressed in terms of partial differential equations in space and time. A possible discretization scheme which incorporates the effective thickness of the layer is presented. Numerical results indicate the validity of the modeling as well as the suggested discretization scheme. Although this model is only verified for a one-dimensional problem, the generalization to higher spatial dimensions is possible since the equation is applied only at the interface. However, tangential variations may need to be considered in those cases. Furthermore, the concept of using the rational functions to approximate the frequency domain response and converting to the time domain may be used to characterize other fine structures.

## APPENDIX

For simplicity, the relative permittivity and permeability are assumed real. For a plane wave normally incident with waveform  $g$ ,

$$E_i = g(\tau + y), \quad \eta_0 H_i = -g(\tau + y). \quad (\text{A1})$$

the reflected and transmitted waves are

$$E_r = f(\tau - y), \quad \eta_0 H_r = f(\tau - y); \quad (\text{A2})$$

$$E_s = p(\tau + \sqrt{\mu_r \epsilon_r} y + \sqrt{\mu_r \epsilon_r} \Delta) - p(\tau - \sqrt{\mu_r \epsilon_r} y - \sqrt{\mu_r \epsilon_r} \Delta); \quad (\text{A3a})$$

$$\eta_0 H_s = -\frac{1}{\eta_r} p(\tau + \sqrt{\mu_r \epsilon_r} y + \sqrt{\mu_r \epsilon_r} \Delta) - \frac{1}{\eta_r} p(\tau - \sqrt{\mu_r \epsilon_r} y - \sqrt{\mu_r \epsilon_r} \Delta); \quad (\text{A3b})$$

In (A2) and (A3), the subscript  $r$  and  $s$  denote the reflected wave and the wave inside the coating, respectively. Note that the boundary condition on the surface of the conductor has been satisfied. Imposing the boundary conditions of continuous tangential electric and magnetic fields at the interface,

$$E = g(\tau) + f(\tau) = p(\tau + \sqrt{\mu_r \epsilon_r} \Delta) - p(\tau - \sqrt{\mu_r \epsilon_r} \Delta), \quad (\text{A4a})$$

$$\eta_0 H = g(\tau) + f(\tau) = -\frac{1}{\eta_r} p(\tau + \sqrt{\mu_r \epsilon_r} \Delta) - \frac{1}{\eta_r} p(\tau - \sqrt{\mu_r \epsilon_r} \Delta). \quad (\text{A4b})$$

In addition, the total tangential electric and magnetic fields are related by:

$$E = 2g(\tau) + \eta_0 H. \quad (\text{A5})$$

Applying the center-differencing and averaging approximations:

$$p(\tau + \sqrt{\mu_r \epsilon_r} \Delta) - p(\tau - \sqrt{\mu_r \epsilon_r} \Delta) \sim 2\Delta \sqrt{\mu_r \epsilon_r} p'(\tau) + \frac{1}{3} \Delta^3 (\mu_r \epsilon_r)^{3/2} p'''(\tau) \quad (\text{A6a})$$

$$p(\tau + \sqrt{\mu_r \epsilon_r} \Delta) + p(\tau - \sqrt{\mu_r \epsilon_r} \Delta) \sim 2p(\tau) + \Delta^2 \mu_r \epsilon_r p''(\tau), \quad (\text{A6b})$$

where "'''" denotes derivative with respect to the argument. Substituting these back into (A4),

$$2g(\tau) = \frac{2}{\eta_r} p(\tau) + 2\Delta \sqrt{\mu_r \epsilon_r} p'(\tau) + \frac{\Delta^2}{\eta_r} \mu_r \epsilon_r p''(\tau) + \frac{\Delta^3}{3} (\mu_r \epsilon_r)^{3/2} p'''(\tau) \quad (\text{A7})$$

$$\eta_0 H = -\frac{1}{\eta_r} [2p(\tau) + \Delta^2 \mu_r \epsilon_r p''(\tau)]. \quad (\text{A8})$$

Substituting (A7) and (A8) to (A5),  $E$  is related to the first and third derivatives of  $p(\tau)$ . Again, using (A8) and ignoring the terms involving derivatives higher than third order by assuming slowly varying field in the time scale of  $\Delta$ :

$$E = -\Delta \mu_r \frac{\partial \eta_0 H}{\partial \tau} + \frac{\Delta^3 \mu_r^2 \epsilon_r}{3} \frac{\partial^3 \eta_0 H}{\partial \tau^3}. \quad (\text{A9})$$

Using Maxwell's equations:

$$E = \Delta \mu_r \frac{\partial E}{\partial y} - \frac{\Delta^3 \mu_r^2 \epsilon_r}{3} \frac{\partial^3 E}{\partial \tau^2 \partial y}.$$

This is what one expects if one expands, in Taylor series, the *tangent* function in (1) and converts the expanded equation to the time domain using the procedure described earlier.

#### REFERENCES

- [1] T. B. A. Senior and J. L. Volakis, "Derivation and application of a class of generalized boundary conditions," *IEEE Trans. Antennas Propagat.*, vol. 37, pp. 1566-1572, Dec. 1989.
- [2] R. Holland and L. Simpson, "Implementation and optimization of the thin-strut formalism in THREDE," *IEEE Trans. Nuclear Sci.*, vol. NS-6, pp. 1625-1630, 1980.
- [3] A. Taflov, K. R. Umashankar, B. Beker, F. Harfoush, and K. S. Yee, "Detailed FD-TD analysis of electromagnetic fields penetrating narrow slots and lapped joints in thick conducting screens," *IEEE Trans. Antennas Propagat.*, vol. 36, p. 247-257, Feb. 1988.
- [4] C. F. Lee, R. T. Shin, and J. A. Kong, "Application of finite-difference time-domain techniques to dispersive media," *Progress in Electromagnetics Research Symp.* Cambridge, MA, July 1991.
- [5] —, *Progress in Electromagnetic Research*, J. A. Kong, Ed., vol. 4, pp. 373-442, New York: Elsevier, 1991.

## Comments on "Criteria for the Onset of Oscillation In Microwave Circuits"

Robert W. Jackson

The paper listed above<sup>1</sup> notes that the device reflection coefficient,  $\Gamma_d(s)$ , in the expression,

$$V^* = \frac{\Gamma_d(s)}{1 - \Gamma_d(s)\Gamma_c(s)} V_i$$

represents the port reflection coefficient of a device which may result in an unstable circuit only *after* connecting it with a resonator having a reflection coefficient,  $\Gamma_c(s)$ . This is an important condition and is somewhat vague as worded. In order to use the Nyquist criterion to determine the stability of the device-circuit combination,  $\Gamma_d$  must have no right half plane poles. This amounts to insuring that the device does not oscillate into the reference impedance (50 ohms for example). If  $\Gamma_d$  has been determined from measurements, presumably the device is not oscillating during the measurement and therefore there are no right half plane poles.

In CAD simulations of possibly unstable circuits, the location of  $\Gamma_d$  poles is not always so clear. For a simple amplifier circuit such as the one described in the above referenced paper, one can assume no right half plane poles in  $\Gamma_d$  if the  $S_{11}$  and/or  $S_{22}$  coefficients of the FET have magnitudes less than one. To see this, consider the partial circuit formed by a 50 ohm termination on port 2 and any passive termination on port 1. If  $|S_{11}| < 1$ , the input termination sees a passive impedance and therefore the partial circuit is stable. Since the partial circuit is stable,  $\Gamma_d$  (50 ohm reference) seen looking in at port 2 has no poles in the right half plane. If, as in the amplifier example<sup>1</sup>,  $\Gamma_d$  has a magnitude greater than 1, the Nyquist criterion as described can then be applied to study the stability effects of various port 2 terminations. In simulations using devices with extra feedback, oscillators for example, often the magnitudes of  $S_{11}$  and  $S_{22}$  are both greater than one and this approach breaks down.

A more generally applicable use of the Nyquist stability criterion has been known for years, but the current widespread use of microwave CAD makes it must easier to apply. As discussed in the literature [1], [2] the admittance between any two nodes in an active circuit cannot have right half plane zeros if the circuit is to be stable. If one were to apply the Nyquist test to such an admittance, the resulting Nyquist locus of points cannot encircle zero in a clockwise sense if the circuit is stable. It is trivial for modern microwave CAD programs to calculate the necessary admittances vs frequency. Polar plotting of admittances is not always available but a quick sketch is easy to do. It should be noted that the number of Nyquist encirclements only gives the *difference* between the number of right half plane zeros and poles in the admittance function. If, for example, the admittance at a particular node pair has an equal number of right half plane poles and zeros, the Nyquist plot would not encircle the origin even though the circuit is unstable. Thus a clockwise encirclement insures instability, but no encirclement does not insure stability. Since admittances at various node

<sup>1</sup>R. W. Jackson, *IEEE Trans. Microwave Theory Tech.*, vol. 40, no. 3, pp. 566-568, Mar. 1992.

# Inverse-scattering view of modal structures in inhomogeneous optical waveguides

Jiqing Xia, Arthur K. Jordan,\* and Jin A. Kong

Department of Electrical Engineering and Computer Science, Massachusetts Institute of Technology,  
Cambridge, Massachusetts 02139

Received March 14, 1991; revised manuscript received September 26, 1991; accepted December 2, 1991

To understand the physical meaning of rational reflection coefficients in inverse-scattering theory for optical waveguide design [J. Opt. Soc. Am. A 6, 1206 (1989)], we studied the relationship between the poles of the transverse reflection coefficient and the modes in inhomogeneous dielectrics. By using a stratified-medium formulation we showed that these poles of the spectral reflection coefficient satisfy the same equation as the guidance condition in inhomogeneous waveguides. Therefore, in terms of wave numbers, the poles are the same as the discrete modes in the waveguide. The radiation modes have continuous real values of transverse wave numbers and are represented by the branch cut on the complex plane. Based on these results, applications of the Gelfand-Levitan-Marchenko theory to optical waveguide synthesis with the rational function representation of the transverse reflection coefficient are discussed.

## 1. INTRODUCTION

The electromagnetic inverse problem is to find unknown parameters of an object from its responses to given electromagnetic signals. The electromagnetic inversion method is an emerging technique in many fields, such as geophysical media and ionosphere probing, medical imaging, nondestructive material characterization, and remote sensing. These applications belong to the identification problem, which is to determine the unknown parameters from measured data. Recently, inversion theory has been applied to synthesis (or design) problems in which the response of the object is not measured but prescribed from design criteria. One important application is the design of dielectric optical waveguides.<sup>1-3</sup> This design problem is to determine the refractive-index profile of a graded-refractive-index guided wave device for given requirements of modal structure. One of the advantages of using a graded-refractive-index optical waveguide is that the core region can be made wider relative to the homogeneous guide. Therefore it is easier to fabricate the guide at optical wavelengths.

For a one-dimensional planar problem, as shown in Fig. 1, the dielectric profile  $\epsilon(x)$  can be obtained from the reflection coefficients  $r$  measured at the surface  $x = 0$ . This is a well-known inverse-scattering problem. In the spectral inverse-scattering theory [Gelfand-Levitan-Marchenko (G-L-M)], closed-form solutions of  $\epsilon(x)$  may be obtained if the reflection coefficient  $r$  is represented by a rational function.<sup>4-7</sup> In the design problem, for given requirements of possible guided modes in the waveguide, the first step is to determine the transverse reflection coefficient on which the spectral inverse-scattering theory (G-L-M) can be applied. This reflection coefficient should contain all the modal information required in the slab. The second step is to apply the inverse theory to solve the index profile. This step has been discussed at great length in the literature, while the first step has received little discussion. An alternative design procedure

is to solve the index profile directly from the modal requirements without constructing a reflection coefficient. That is not discussed in this paper. The motivation for using a reflection coefficient here is to utilize the previous results in inverse scattering, especially the rational function representation of the reflection coefficient for closed-form solutions. The purpose of this paper is to investigate the feasibility of designing optical waveguides by constructing a transverse reflection coefficient as a starting point.

There are two types of measurement in one-dimensional frequency-domain problems, frequency diversity and angle diversity. These correspond to the two independent variables, the angular frequency  $\omega$  and a component of the wave vector. If a layered model is used to describe the inhomogeneous medium, owing to the phase-matching condition on the boundaries between layers,  $k_x$  will be independent of  $x$ , i.e., all the layers have the same  $k_x$ . Since  $k_y = 0$ , there are only two components in the wave vector  $\mathbf{k}$ ,  $k_x$  and  $k_z$ . The components of a wave vector satisfy the dispersion relation in each layer. Therefore only one component is independent. In region  $\epsilon_1$  in Fig. 1 we choose  $k_{1x}$  as the independent variable. The transverse reflection coefficient is written as a function of  $k_{1x}$  and  $\omega$ , i.e.,  $r(k_{1x}, \omega)$ , which is consistent with the notation in previous work,<sup>1</sup> where  $r(k_{1x})$  is written as  $r(k)$ . In optical-waveguide-design problems, since the operating frequency is usually fixed,  $r(k_{1x}, \omega)$  reduces to  $r(k_{1x})$ . This is different from the profile identification problem in Refs. 5 and 7, where, for fixed normal incidence,  $k_{1x} = k = \omega/c$ ,  $r(\omega)$  is actually considered. In this paper we discuss only  $r(k_{1x})$  for the waveguide-design problem. Furthermore, the rational function representation of  $r(k_{1x})$ , where the poles of the reflection coefficient are related to the electromagnetic modes supported by the waveguide, is considered. The correspondence between the poles and the modes is studied.

An integral formulation known as the Sommerfeld integral<sup>8-10</sup> is usually used in calculating the fields of a dipole

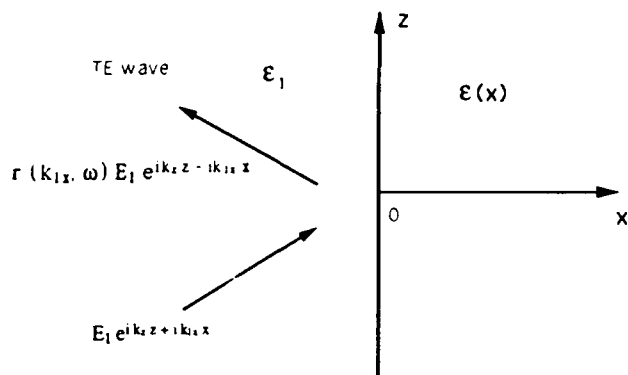


Fig. 1. One-dimensional inverse-scattering problem.

in layered media. It is a well-known result that the poles of the Sommerfeld integrand correspond to the modes in the media. This result can be obtained from the residue theorem in the theory of complex variables. For instance, the Green's function in a layered medium can be written as

$$G(\mathbf{r}, \mathbf{r}') = \iint_{-\infty}^{\infty} d\mathbf{k}_s [A(\mathbf{k}_s) + r(\mathbf{k}_s)B(\mathbf{k}_s)] \times \exp[i\mathbf{k}_s \cdot (\mathbf{r}_s - \mathbf{r}'_s)], \quad (1)$$

where  $\mathbf{r}_s = \hat{y}y + \hat{z}z$ ,  $d\mathbf{k}_s = dk_x dk_z$ , and  $\mathbf{k}_s = \hat{y}k_y + \hat{z}k_z$  is the wave vector in the plane of the layers (Fig. 1).  $\mathbf{k}_s$  reduces to  $\hat{z}k_z$  since  $k_y = 0$ .  $A(\mathbf{k}_s)$  and  $B(\mathbf{k}_s)$  are functions related to the medium. Surface-wave modes are the poles of the Green's function, which are from the poles of the transverse reflection coefficient  $r(k_z)$ ; here  $k_z$  is chosen as the independent wave number. Studying the Green's function in the Sommerfeld integral is one way to obtain the relation between the poles of  $r$  and the modes in the medium. In constructing a rational reflection coefficient in the design problem, it is critical to relate the guidance condition to the pole condition of the reflection coefficient. To understand the pole condition of  $r$  in terms of the field distribution, in this paper we propose another approach, which is based on the analysis of the electromagnetic reflection coefficient and the guidance condition of a layered medium.

For a given inhomogeneous medium, the reflection coefficient is derived in recursive form by using the layered-medium model. The pole condition for the reflection coefficient can then be obtained. A mode is a possible field structure in certain physical systems; electromagnetic modes are the possible solutions of Maxwell's equations with certain boundary conditions. In a layered medium the guidance condition is a necessary condition for the existence of guided modes derived from the boundary conditions. We show that the pole equation for the reflection coefficient is the same as the guidance condition in the medium. Thus the poles of the reflection coefficient are indeed the modes of the guiding structure. The starting point of this study is a single-layer medium that is a homogeneous dielectric slab waveguide. In this simple case the possible solutions for the pole equation can be fully analyzed. For a general  $N$ -layer medium, a proof is given that the guidance conditions in all the layers are equivalent. Furthermore, this guidance condition is shown to be equivalent to the pole equation of the total

reflection coefficient. The solutions of the guidance condition give both the guided and the leaky modes. Radiation modes are not poles of the reflection coefficient. The results on the pole-mode relation are used to interpret the poles of the rational reflection coefficient in the inverse-scattering problem applied to optical waveguide design.

## 2. HOMOGENEOUS DIELECTRIC WAVEGUIDE

To find the relationship between the modal structure and the transverse reflection coefficient, we first analyze the homogeneous dielectric waveguide shown in Fig. 2. Although this is the simplest case of general dielectric waveguides and has been discussed extensively, it serves the purpose of illustrating the results in an analytic form.

The propagation direction is  $+z$  in Fig. 2. The  $x$  direction is called the transverse direction. The reflection coefficient  $r(k_{1x}, \omega)$  is obtained by solving the direct scattering problem for an incident plane wave,<sup>8</sup>

$$r(k_{1x}, \omega) = \frac{R_{-10} + R_{01} \exp(i2k_z d)}{1 + R_{-10} R_{01} \exp(i2k_z d)}, \quad (2)$$

where  $k_z$  is the wave number along the  $z$  direction,  $\omega$  is the angular frequency,  $d$  is the thickness of the slab, and  $R_{ij}$  is the Fresnel reflection coefficient for a plane wave incident from medium ( $i$ ) to medium ( $j$ ). Since

$$R_{-10} = -R_{01}, \quad (3)$$

the poles are determined by

$$R_{01}^2 \exp(i2k_z d) = 1 \quad (4)$$

for the transverse-electric (TE) wave case, where

$$R_{01} = \frac{k_x - k_{1x}}{k_x + k_{1x}}. \quad (5)$$

The dispersion relations

$$k_{1x}^2 + k_{1z}^2 = k_1^2, \quad (6)$$

where  $k_{1z} = k_z$ , and

$$k_x^2 + k_z^2 = k^2 \quad (7)$$

need to be used in solving Eq. (4);  $k_z$  is the same in all media owing to the phase-matching condition. It is easy

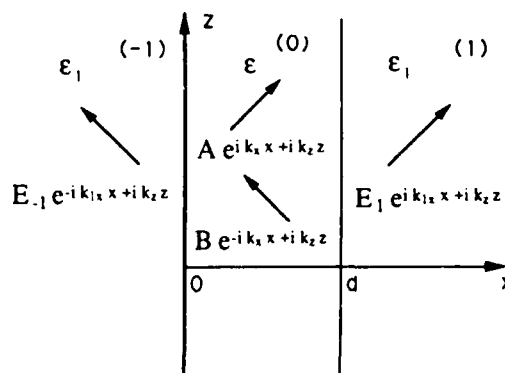


Fig. 2. Mode diagram for discrete modes in slab waveguide.

to prove that

$$r(k_{1x} = 0) = -1, \quad (8)$$

which is the normalization condition of the rational reflection coefficient.

The poles of  $r(k_{1x})$  are those values of  $k_{1x}$  that satisfy Eq. (4). At the poles  $r \rightarrow \infty$ , which indicates a self-resonant structure. When a plane wave is incident upon the slab with real  $k_{1x}$ , owing to conservation of energy  $|r| \leq 1$ . This is because, for real values of  $k_{1x}$  and  $k_x$ ,  $|R_{01}| \leq 1$ , the pole condition will not be satisfied. The poles of  $r(k_{1x})$  are complex.

In Fig. 2 the guided modes are defined as the waves propagating along the  $+z$  direction and exponentially decaying along the transverse direction outside the slab. The modes in the dielectric waveguide are determined from the boundary conditions. For a TE wave, the  $E_y$  fields in the three regions can be expressed as

$$\begin{aligned} \vec{E}_{-1} &= E_{-1} \exp(ik_z z) \exp(-ik_{1x} x) \\ &\text{for region } (-1), x < 0, \end{aligned} \quad (9a)$$

$$\begin{aligned} \vec{E}_0 &= \exp(ik_z z) [A \exp(ik_x x) + B \exp(-ik_x x)] \\ &\text{for region } (0), 0 < x < d, \end{aligned} \quad (9b)$$

$$\begin{aligned} \vec{E}_1 &= E_1 \exp(ik_z z) \exp(ik_{1x} x) \\ &\text{for region } (1), x > d. \end{aligned} \quad (9c)$$

At  $x = 0$  in region (0), the right-going wave is due to the reflection of the left-going wave at the boundary, which yields  $A = BR_{0(-1)}$ . With  $R_{0(-1)} = -R_{-10}$  and using Eq. (3), we have

$$A = BR_{01}. \quad (10)$$

At  $x = d$  in region (0), the left-going wave is due to the reflection of the right-going wave at this boundary; thus

$$B \exp(-ik_x d) = A \exp(ik_x d) R_{01}, \quad (11)$$

and combining Eqs. (10) and (11) yields

$$\exp(2ik_x d) R_{01}^2 = 1. \quad (12)$$

Equation (12) is a transverse resonance condition satisfied by any field distribution of Fig. 2 (as we see in matching boundary conditions) and is known as the guidance condition.<sup>8,10</sup> This equation is the same as Eq. (4). Thus the guidance condition is equivalent to the pole condition for the reflection coefficient. Equation (12) can also be obtained by using the boundary conditions at  $x = 0$  and  $x = d$  for both the  $\mathbf{E}$  and the  $\mathbf{H}$  fields from Eq. (9).

For a fixed real angular frequency  $\omega$  there is only one unknown in Eq. (12). This unknown can either be  $k_{1x}$  or  $k_x$ . The possible solutions that satisfy the guidance condition [Eq. (12)] can be discussed in the following three cases of  $k_x$ :

### Case 1. $k_x$ is Real

(a)  $k_{1x}$  is also real. This gives  $|\exp(i2k_x d)| = 1$  and  $|R_{01}| < 1$ . This case cannot satisfy guidance-condition equation (12). We assume that  $\epsilon > \epsilon_1$ . For  $\epsilon_1 > \epsilon$ , since  $k_{1x}^2 = k_x^2 + k_1^2 - k^2$ ,  $k_x$  and  $k_{1x}$  will both be real, as in the present case. Thus there is no discrete mode for  $\epsilon_1 > \epsilon$ .

(b)  $k_{1x}$  is purely imaginary. Here  $k_1^2 - k^2 = k_{1x}^2 -$

$k_x^2 < 0$ ,  $\epsilon_1 < \epsilon$ , and  $k_{1x}^2 = k_x^2 + k_1^2 - k^2$  is real. Thus, if  $k_{1x}$  is complex,  $k_{1x}$  has to be purely imaginary. In this case  $|\exp(i2k_x d)| = 1$ ,  $|R_{01}| = 1$ , so that it is possible for the guidance condition [Eq. (12)] to have a finite number of solutions with discrete  $k_x$  values.  $k_x^2 = k_{1x}^2 + k^2 - k_1^2 < k^2 - k_1^2$ . The proper  $k_{1x}$  values are on the positive imaginary axis on the complex  $k_{1x}$  plane. Since  $k_{1x}$  is positive imaginary, the wave is decaying along the  $x$  direction outside the slab. There are improper  $k_{1x}$  solutions on the negative imaginary axis of the  $k_{1x}$  plane. The solution of Eq. (12) in the present case also includes the trivial root  $k_x = 0$ , which gives a zero field everywhere. From Eq. (10), if  $k_x = 0$ ,  $R_{01} = -1$  and then  $A = -B$ . From Eq. (9),  $\vec{E}_0 = 0$ . Since  $E_y$  is continuous at the boundaries,  $\vec{E}_{-1} = 0$  and  $\vec{E}_1 = 0$ .

### Case 2. $k_x$ is Purely Imaginary

This implies that  $k_x^2 > k^2$  and  $k_x$  is real.

(a)  $\epsilon > \epsilon_1$ ,  $k > k_1$ , so that

$$k_{1x}^2 = k_x^2 - (k^2 - k_1^2) < k_x^2 < 0, \quad (13)$$

and  $k_{1x}$  is also an imaginary number. Let  $k_x = ia$  and  $k_{1x} = ia_1$  for decaying waves outside the slab, and  $a_1 > 0$  and  $|a_1| > |a|$ .

(i)  $a > 0$ ,  $|R_{01}| < 1$ , and  $\exp(-2ad) < 1$ , which is not a possible solution to Eq. (12).

(ii)  $a < 0$ ,  $|R_{01}| > 1$ , and  $\exp(-2ad) > 1$ , which is also not a possible solution to Eq. (12).

(b)  $\epsilon < \epsilon_1$ ,  $k < k_1$ .

(i)  $k_{1x}$  is real,  $k_1 > k_x$ .  $|R_{01}| = 1$ , and  $|\exp(-2ad)| > 1$  or  $< 1$ . This is not a possible solution for Eq. (12).

(ii)  $k_{1x}$  is imaginary,  $k_1 < k_x$ , the same as in case 2(a).

From case 2 it can be concluded that purely imaginary  $k_x$  cannot be the poles of the reflection coefficient.

### Case 3. $k_x$ Has Both Real and Imaginary Parts

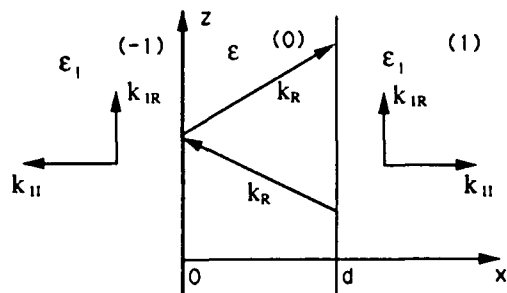
Since  $k_x^2 = k^2 - k_z^2$ ,  $k_x$  is also complex, and  $k_x = k_x' + ik_x''$ . Since the propagation direction is  $+z$ ,  $k_z' > 0$  and  $k_z'' > 0$ . Defining  $k_x = k_x' + ik_x''$  and from  $k_x^2 = k^2 - k_z^2 = k^2 - k_z'^2 + k_z''^2 - i2k_z'k_z''$ , we get  $k_x'k_x'' = -k_z'k_z''$ . For the same reason,  $k_{1x} = k_{1x}' + ik_{1x}''$ , and  $k_{1x}^2 = k_1^2 - k_x^2 = k_1^2 - k_x'^2 + k_x''^2 - i2k_x'k_x''$  and  $k_{1x}'k_{1x}'' = -k_x'k_x''$ . Since  $k_z'k_z'' > 0$  and  $k_x'k_x'' < 0$ ,  $k_{1x}'k_{1x}'' < 0$ . Outgoing waves require that  $k_{1x}' > 0$  in regions (-1) and (1); hence  $k_{1x}'' < 0$ .

There are two equivalent cases for  $k_x, k_x' > 0$  and  $k_x'' < 0$ . We choose  $k_x' > 0$  and  $k_x'' < 0$ . This means that  $|\exp(-2k_x'' d)| > 1$ . If Eq. (12) is satisfied,  $|R_{01}| < 1$ . Since

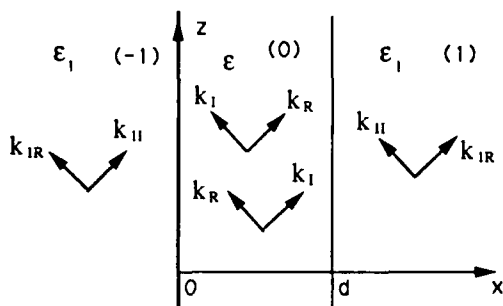
$$|R_{01}| = \left| \frac{(k_x' - k_{1x}')^2 + (k_x'' - k_{1x}'')^2}{(k_x' + k_{1x}')^2 + (k_x'' + k_{1x}'')^2} \right|^{1/2} \quad (14)$$

gives  $|R_{01}| < 1$ , this is a possible solution. These solutions are called the leaky modes since the power leaks away from the surface. As is illustrated in Fig. 3(b), outside the slab the wave is growing away from the waveguide along the  $x$  direction but decaying along the  $+z$  direction. In this mode diagram, the total wave is propagating along the real part of the wave vector,  $\mathbf{k}_{1R}$ , and decaying along the imaginary part of the wave vector,  $\mathbf{k}_{1I}$ .

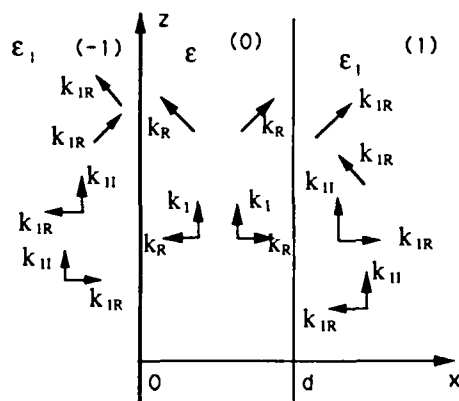
In conclusion, the possible solutions to the guidance condition [Eq. (12)] are discrete. These solutions can be classified into two cases:



(a) guided modes



(b) leaky modes



(c) radiation modes

Fig. 3. Wave vectors in slab waveguide for (a) guided modes, (b) leaky modes, and (c) radiation modes.

(1) Guided modes.  $k_x$  is real,  $k_x^2 < k^2 - k_1^2$ , and  $k_{1x}$  is purely imaginary with a positive imaginary part.

These are also called the surface-wave modes because the wave is guided inside the two surfaces. Outside the surfaces the wave decays exponentially. This surface wave is associated with the total internal reflection at the surface boundaries.

(2) Leaky modes.  $k_x$  is complex, and  $k_{1x}' > 0$ ,  $k_{1x}'' < 0$ .

There are an infinite number of leaky modes that are also discrete. They usually do not contribute to the complete eigenfunction set of field solutions of the open

waveguide. Leaky modes lie on the improper Riemann sheet [which is separated from the proper Riemann sheet by the cut of  $\text{Im}(k_{1x}) = 0$ ] of the complex  $k_x$  plane. Most of them will not be excited. A finite number of leaky modes may contribute to the total field when the excitation condition is satisfied (Ref. 8, p. 326). In this case the leaky-mode amplitudes will not diverge.

The cutoff frequency of a guided mode is determined by the condition  $k_x^2 \geq k^2 - k_1^2$ . At cutoff,  $k_x = (k^2 - k_1^2)^{1/2}$ ,  $k_{1x} = 0$ , and  $R_{01} = 1$ . From the guidance condition [Eq. (12)],  $k_x = m\pi/d$  for  $m = 0, \pm 1, \pm 2, \dots$ . Hence

$$k_{c0} = \frac{m\pi}{d} \frac{1}{(\epsilon_r - \epsilon_{1r})^{1/2}}$$

The cutoff frequencies for the TE<sub>m</sub> [also true for transverse-magnetic (TM<sub>m</sub>)] modes are

$$f_{cm} = \frac{cm}{2d} \frac{1}{(\epsilon_r - \epsilon_{1r})^{1/2}}$$

As the frequency decreases, when  $f < f_{cm}$ , the  $m$ th guided mode will be cut off. As a solution to Eq. (12) this mode becomes a leaky mode that has both real and imaginary parts in  $k_x$ . The leaky mode is different from a radiation mode.

The radiation modes are defined as possible field distributions in the slab with real  $k_{1x}$  in regions (-1) and (1). These modes carry energy infinitely far away and are not guided locally. In terms of the spectral parameters  $k_{1x}$ , the difference between radiation modes and leaky modes is that leaky modes have an imaginary part  $k_{1x}'' < 0$  and radiation modes have a continuous real  $k_{1x}$ .

As discussed above, it is impossible to have fields of Eqs. (9) with real  $k_{1x}$ ; hence the radiation modes are not possible with the field structures of Fig. 2. The radiation modes are not poles of the reflection coefficient  $r(k_{1x}, \omega)$ .

Another possible field structure is shown in Fig. 4, where

$$\begin{aligned} \vec{E}_{-1} = & E_{-1} \exp(ik_z z) \exp(ik_{1x} x) + r(k_{1x}) E_{-1} \exp(ik_z z) \\ & \times \exp(-ik_{1x} x) \end{aligned} \quad \text{for region } (-1), x < 0, \quad (15a)$$

$$\vec{E}_0 = \exp(ik_z z) [A \exp(ik_x x) + B \exp(-ik_x x)] \quad \text{for region } (0), 0 < x < d, \quad (15b)$$

$$\vec{E}_1 = E_1 \exp(ik_z z) \exp(ik_{1x} x) \quad \text{for region } (1), x > d, \quad (15c)$$

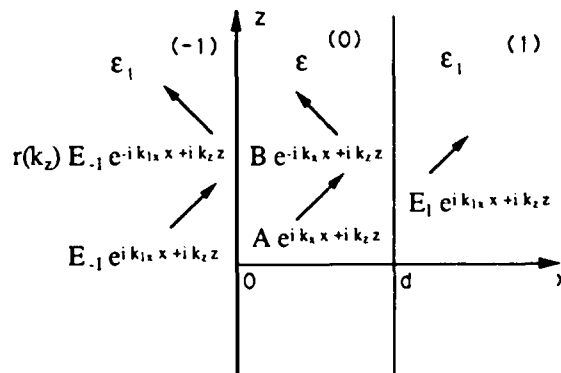


Fig. 4. Mode diagram for radiation modes in slab waveguide.

Note that  $\text{Re}(k_{1z}) > 0$ , and the field in region (-1) has an incident term that is different from the one in Fig. 2. With this field distribution, at  $x = d$ ,  $B \exp(-ik_x d) = A \exp(ik_x d) R_{01}$  is still valid. However, at  $x = 0$ ,  $A = BR_{01} + T_{10} E_{-1}$ , which is different from Eq. (10). This can also be checked by matching the boundary conditions on  $\mathbf{E}$  and  $\mathbf{H}$  at  $x = 0$ . Equation (12) does not hold in this case, so that  $k_{1z}$  can be real numbers; therefore the radiation modes exist. The modal structure of Fig. 4 is equivalent to putting a source in region (-1) so that the wave is incident from  $x = -\infty$ . Now the  $k_{1z}$  value can change continuously. Radiation modes form the continuous spectrum of eigenfunctions of a dielectric waveguide. Continuous radiation modes along with the discrete guided modes, in general, form a complete eigenfunction set in which the field from an arbitrary source can be expanded.<sup>9</sup> The continuous spectrum also includes the radiation modes that are due to incident waves from the right-hand region (1). The analogy in quantum mechanics is that the unbound states are relevant to scattering problems; such problems characteristically involve a wave that is incident from the exterior region.<sup>11</sup> Here  $k_{1z}^2 = k_1^2 - k_z^2 > 0$ , and there are two cases to be considered:

*Case (1)*  $k_z$  is real.  $k_z < k_1$ , and  $k_{1z} < k_1$ .

This corresponds to the case in which the power is incident from the exterior regions, (-1) or (1) in Fig. 4.

*Case (2)*  $k_z$  is purely imaginary. This means that  $k_{1z} > k_1$ .

This case is sometimes referred as the evanescent mode<sup>3,8,9</sup> since the wave is exponentially decaying along the propagation direction  $+z$ .

The radiation modes lie on the Sommerfeld branch cut. The same results are derived from the Green's-function approach. These radiation modes are illustrated in Fig. 3(c). Note that  $\mathbf{k}_I$  is always orthogonal to  $\mathbf{k}_R$ , which can be proved by calculating  $\mathbf{k}_I \cdot \mathbf{k}_R$  and using  $k_x' k_x'' = -k_z' k_z''$ , so that  $\mathbf{k}_I \cdot \mathbf{k}_R = 0$ .

In summary, the modal structure of a dielectric slab (Fig. 5) shows the pole positions in the complex plane corresponding to the modes for a fixed real  $\omega$ . In Fig. 5, only half of the complex planes are shown, owing to the definition of  $\text{Re}(k_x) \geq 0$ ,  $\text{Re}(k_z) \geq 0$ , and  $\text{Re}(k_{1z}) \geq 0$ . Note that the radiation modes lie on the Sommerfeld branch cut and that the leaky modes are on the improper Riemann sheet.

For numerical examples, the guided and the leaky modes are calculated in the slab waveguide for two different frequencies. The first one is at microwave frequency  $f = 12$  GHz,  $d = 1$  cm,  $\epsilon_r = 10$ , and  $\epsilon_{1r} = 1$ . Here  $k_0 = 251 \text{ m}^{-1}$  and  $(k^2 - k_1^2)^{1/2} = 754 \text{ m}^{-1}$ . For the TE polarization, by calculating the cutoff frequencies,  $f_{cm} = 5.0$  m GHz, we find three guided modes. These are  $\text{TE}_0$ ,  $\text{TE}_1$ , and  $\text{TE}_2$ . Table 1 shows the calculated wave numbers,  $k_x$ ,  $k_{1z}$ , and  $k_z$ , for the guided modes and some leaky modes.

Another example is for the optical frequency,  $f = 2.255639 \times 10^{14}$  Hz, corresponding to  $\lambda_0 = 1.33 \text{ } \mu\text{m}$ . The parameters are  $d = 2.5 \text{ } \mu\text{m}$ ,  $\epsilon_r = 12.96$  ( $n = 3.6$ ),  $\epsilon_{1r} = 12.6025$  ( $n_1 = 3.55$ ),  $k_0 = 4.7242 \times 10^6 \text{ m}^{-1}$ ,  $(k^2 - k_1^2)^{1/2} = 2.8267 \times 10^6 \text{ m}^{-1}$ ,  $k_1 = 16.78 \times 10^6 \text{ m}^{-1}$ , and  $k = 17.02 \times 10^6 \text{ m}^{-1}$ . The cutoff frequencies are  $f_{cm} = 1.0 \times 10^{14} \text{ m Hz}$ . The results are shown in Table 2.

### 3. GENERAL INHOMOGENEOUS WAVEGUIDE

In this section we analyze a general inhomogeneous waveguide, using a layered model. The results of Section 2 are generalized from the one-layer slab to an  $N$ -layer medium shown in Fig. 6. Assuming that a TE wave is incident in region (-1) from the left, the reflection coefficient can be obtained in a recursive form (Ref. 8, p. 130, Sec. 3.3; note that here we use the coordinate system as in Sec. 3.5) as

$$r(k_{1z}, \omega) = \frac{B_{-1}}{A_{-1}}, \quad (16)$$

where  $A_{-1}$  and  $B_{-1}$  are the wave amplitudes shown in Fig. 6:

$$r(k_{1z}, \omega) = \frac{1}{R_{-10}} + \frac{(1 - 1/R_{-10}^2)}{1/R_{-10} + B_0/A_0}. \quad (17)$$

The poles are the zeros of the pole equation

$$\frac{B_0}{A_0} = -\frac{1}{R_{-10}}. \quad (18)$$

Matching the boundary conditions of  $\mathbf{E}$  and  $\mathbf{H}$  at  $x = d_1$  gives

$$\frac{B_0}{A_0} = \frac{\exp(i2k_x d_1)}{R_{01}} + \frac{(1 - 1/R_{01}^2) \exp[i2(k_{1z} + k_z) d_1]}{1/R_{01} \exp(i2k_{1z} d_1) + B_1/A_1}. \quad (19)$$

Here the poles of  $B_0/A_0$  are not the poles of  $r(k_{1z}, \omega)$  be-

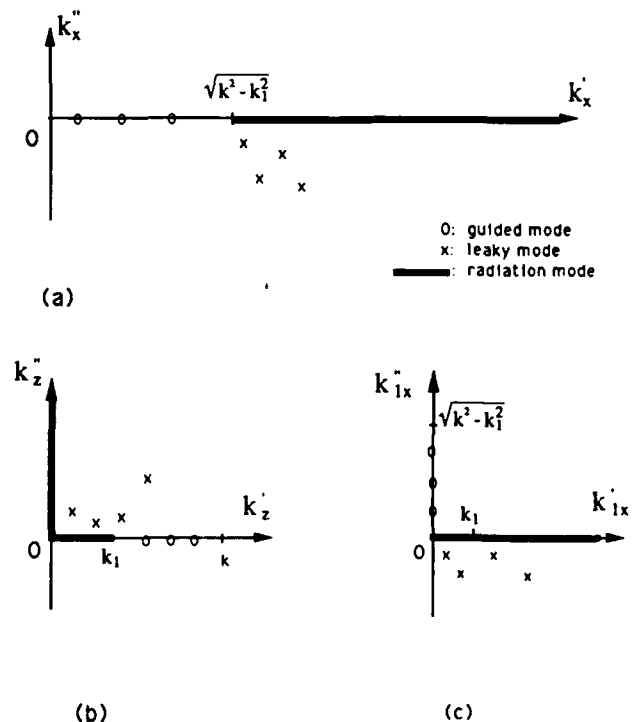


Fig. 5. Discrete and continuous modes shown in complex (a)  $k_x$ , (b)  $k_z$ , and (c)  $k_{1z}$  planes.

**Table 1. Modes of Slab Waveguide at 12 GHz**

Modes	$k_x(\text{m}^{-1})$	$k_{1x}(\text{m}^{-1})$	$k_z(\text{m}^{-1})$
Guided			
TE <sub>0</sub>	247.36	i712.81	755.87
TE <sub>1</sub>	487.74	i575.66	628.20
TE <sub>2</sub>	702.79	i274.51	372.30
Leaky (examples)			
1	892.53 - i130.58	511.96 - i227.64	253.53 + i459.69
2	1530.85 - i271.30	1340.39 - i309.85	315.16 + i1317.84
3	3745.05 - i458.58	3669.45 - i468.02	469.11 + i3660.96

**Table 2. Modes of Optical Slab Waveguide**

Modes	$k_x(10^6 \text{ m}^{-1})$	$k_{1x}(10^6 \text{ m}^{-1})$	$k_z(10^6 \text{ m}^{-1})$
Guided			
TE <sub>0</sub>	0.9749	i2.6532	16.9909
TE <sub>1</sub>	1.9170	i2.0772	16.9106
TE <sub>2</sub>	2.7267	i0.7450	16.7990
Leaky (examples)			
1	3.5616 - i0.6090	2.2858 - i0.9489	16.6537 + i0.1302
2	4.8427 - i0.9323	3.9845 - i1.1331	16.3443 + i0.2762
3	6.1177 - i1.1450	5.4565 - i1.2837	15.9286 + i0.4398
4	7.3889 - i1.3077	6.8474 - i1.4111	15.3997 + i0.6274
5	8.6573 - i1.4406	8.1975 - i1.5214	14.7474 + i0.8457

cause at these values  $r$  is finite. For an arbitrary layer  $l$ ,

$$\frac{B_l}{A_l} = \frac{\exp(i2k_{lx}d_{l+1})}{R_{l(l+1)}} + \frac{[1 - 1/R_{l(l+1)}^2]\exp[i2(k_{l+1}x + k_{lx})d_{l+1}]}{1/R_{l(l+1)} \exp[i2k_{l+1}x d_{l+1}] + B_{l+1}/A_{l+1}}, \quad (20)$$

$$\frac{A_l}{B_l} = \frac{\exp(-i2k_{lx}d_l)}{R_{l(l-1)}} + \frac{[1 - 1/R_{l(l-1)}^2]\exp[-i2(k_{l-1}x + k_{lx})d_l]}{1/R_{l(l-1)} \exp[-i2k_{l-1}x d_l] + A_{l-1}/B_{l-1}}. \quad (21)$$

For the last layer  $n = t - 1$ ,

$$\frac{B_n}{A_n} = R_n \exp(i2k_{nx}d_n). \quad (22)$$

A direct result from Eq. (17) with  $R_{-10} = -1$  is the normalization condition for general inhomogeneous media,

$$r(k_{1x} = 0) = -1. \quad (23)$$

The modes in the medium are studied by assuming a TE wave with  $A_{-1} = 0$  in Fig. 6. A guided wave has a real  $k_x$  and decays exponentially in regions (0) and (t) away from the waveguide; its energy is confined in the layered region, with the thickness of the inhomogeneous region  $d$ , assumed to be finite. If the  $\epsilon(x)$  approaches a constant as  $x \rightarrow \infty$ , an infinitely extended medium can be reduced to an equivalent finite-thickness medium.

The  $E_y$  fields in different regions can be written as

$$E_{-1} = B_{-1} \exp(ik_z z) \exp(-ik_{-1x} x) \quad \text{for region } (-1), x < 0, \quad (24a)$$

$$E_0 = \exp(ik_z z) [A_0 \exp(ik_x x) + B_0 \exp(-ik_x x)] \quad \text{for region } (0), 0 < x < d_1, \quad (24b)$$

$$E_1 = \exp(ik_z z) [A_1 \exp(ik_{1x} x) + B_1 \exp(-ik_{1x} x)] \quad \text{for region } (1), d_1 < x < d_2, \quad (24c)$$

$$E_n = \exp(ik_z z) [A_n \exp(ik_{nx} x) + B_n \exp(-ik_{nx} x)] \quad \text{for region } (n), d_n < x < d_t, \quad (24d)$$

$$E_t = A_t \exp(ik_z z) \exp(ik_{tx} x) \quad \text{for region } (t), x > d_t. \quad (24e)$$

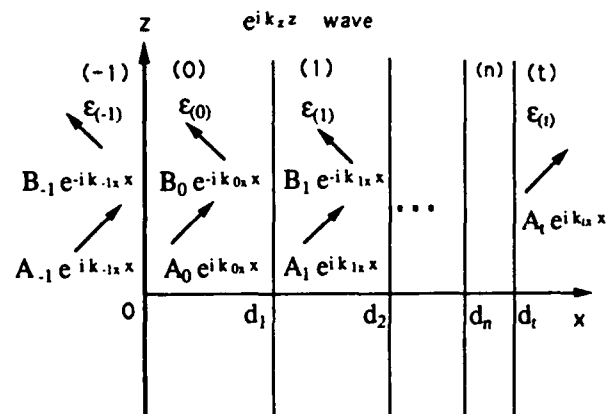


Fig. 6. Mode diagram in inhomogeneous medium.

The necessary condition for the existence of any field distribution in Fig. 6 is the guidance condition in each layer. For layer ( $l$ ),

$$R_{-l}^l R_{-l}^{-l} = 1, \quad (25)$$

where  $R_{-l}^l = B_l/A_l$  and  $R_{-l}^{-l} = A_l/B_l$  are in recursive forms [Eqs. (20) and (21)].

For  $l = 0$ , the guidance condition is

$$R_{-0}^0 R_{-0}^{-0} = 1. \quad (26)$$

Matching the boundary conditions for the **E** and **H** at the boundaries gives

$$R_{-0}^0 = \frac{B_0}{A_0} = \frac{\exp(i2k_x d_1)}{R_{01}} + \frac{(1 - 1/R_{01}^2)\exp[i2(k_{1x} + k_x)d_1]}{1/R_{01}\exp(i2k_{1x}d_1) + B_1/A_1}, \quad (27)$$

$$R_{-0}^{-0} = \frac{A_0}{B_0} = -R_{-10}. \quad (28)$$

It is easy to see that the guidance condition for layer (0) is the same as the pole equations (18) and (19).

Next we show that all the other layers have the same guidance condition or, equivalently, that for any layers  $l$  and  $l - 1$  the guidance conditions are the same. The guidance condition for layer ( $l$ ) is

$$\frac{B_l}{A_l} \left( \frac{\exp(-i2k_{lx}d_l)}{R_{l,l-1}} + \frac{[1 - 1/R_{l,l-1}^2]\exp\{-i2[k_{l-1x} + k_{lx}]d_l\}}{1/R_{l,l-1}\exp[-i2k_{l-1x}d_l] + A_{l-1}/B_{l-1}} \right) = 1, \quad (29)$$

and the guidance condition for layer ( $l - 1$ ) is

$$\left( \frac{\exp[i2k_{l-1x}d_l]}{R_{l-1,l}} + \frac{[1 - 1/R_{l-1,l}^2]\exp[i2[k_{lx} + k_{l-1x}]d_l]}{1/R_{l-1,l}\exp(i2k_{lx}d_l) + B_l/A_l} \right) \frac{A_{l-1}}{B_{l-1}} = 1. \quad (30)$$

Although Eq. (30) appears different from the condition in layer ( $l$ ), Eq. (29), it can be shown that Eqs. (29) and (30) are equivalent. They both can be reduced to an identical equation. Equation (30) can be rewritten as

$$\frac{B_l}{A_l} \left( \frac{[1 - 1/R_{l-1,l}^2]\exp[i2[k_{lx} + k_{l-1x}]d_l]}{-\exp[i2k_{l-1x}d_l]/R_{l-1,l} + B_{l-1}/A_{l-1}} - \frac{1}{R_{l-1,l}\exp(i2k_{lx}d_l)} \right)^{-1} = 1, \quad (31)$$

which can be further simplified as

$$\frac{B_l}{A_l} \left( \frac{(B_{l-1}/A_{l-1})R_{l-1,l}\exp\{-i2[k_{lx} + k_{l-1x}]d_l\} + \exp(-i2k_{lx}d_l)}{B_{l-1}/A_{l-1}\exp[-i2k_{l-1x}d_l] + R_{l,l-1}} \right) = 1. \quad (32)$$

Through algebraic simplification, Eq. (29) can also be written in the same form as Eq. (32). Thus Eqs. (29) and (30) are equivalent. We have just shown that for all layers  $l$  the guidance conditions are the same. This guidance condition is the same as the pole equation [Eq. (18)], so

that the poles represent the modes in the inhomogeneous core region of the waveguide.

Equations (29) and (30) are the conditions that any field distribution of Fig. 6 must satisfy. Possible solutions of Eq. (18) can be studied in detail as in the single-slab case. The results can be summarized into two cases: (1) guided modes, with purely imaginary  $k_{-1x}$  and  $k_{lx}$ , and (2) leaky modes, with  $k_{-1x}$  and  $k_{lx}$  having both real and imaginary parts. The guided and the leaky modes are discrete. Again, the radiation modes do not satisfy the pole equation [Eq. (18)], so that radiation modes are not poles of the reflection coefficient  $r(k_{1x}, \omega)$ . Radiation modes require that there be a wave incident from region ( $-1$ ) or region ( $l$ ), where  $k_{-1x}$  and  $k_{lx}$  are real numbers that can vary continuously from 0 to  $k_{-1}$  and 0 to  $k_l$ , respectively. Since the fields in one layer are dependent on the fields in all the other layers, the waves are considered to be guided in all the layers rather than in a single layer. For a continuously varying  $\epsilon(x)$ , the layered model can also be used by making each layer sufficiently thin. All the above results are valid for continuous inhomogeneous media.

#### 4. IMPLICATIONS FOR INVERSE PROBLEMS

Inverse-scattering problems are concerned with the reconstruction of the physical properties of unknown objects from information contained in their scattering data. In contrast, direct-scattering problems are concerned with determining the scattered fields from known physical properties. In inverse problems, the scattering data  $r(k_{1x}, \omega)$  are basically a set of measurements that relate  $r$  to  $k_{1x}$  or  $\omega$ . To apply the G-L-M inverse-scattering theory, we approximate  $r(k_{1x}, \omega)$  as a closed-form function. One example is that the reflection coefficient  $r(k_{1x}, \omega)$  is represented by a rational function of  $k_{1x}$  or  $\omega$ , and  $r(k_{1x}, \omega)$  is prescribed to have a finite number of poles and zeros; typically for a good approximation many poles and zeros may be needed, similar to circuit network synthesis.<sup>12</sup> Closed-form solutions of the G-L-M integral equation of inverse-scattering theory can be obtained for some rational functions of  $r(\omega)$ .<sup>7</sup> These closed-form solutions are important not only in providing a benchmark for other numerical methods but in solving synthesis problems.

As was discussed in Section 1, there are two kinds of inverse profile problem, the identification and the synthesis problems. In practical profile identification problems it may be difficult to determine from the measured data the functional form of  $r(k_{1x}, \omega)$  that is determined by the unknown permittivity profile. Although the poles and the zeros of  $r(k_{1x}, \omega)$  can be obtained by using Bode diagram techniques together with analytic function extension methods, the rational function approach is more

appropriate for synthesis problems. The synthesis problem is to determine the permittivity profile needed to produce a prescribed reflection coefficient  $r(k_{1x}, \omega)$ . In the optical-waveguide-synthesis problem, the relevant parameters are modeled by continuous functions<sup>13</sup>; in the

present example we use the transverse reflection coefficient  $r(k_{1x})$ . Since  $r(k_{1x})$  will be in general combinations of transcendental functions, which is evident from our discussion of direct scattering, we rely on standard electrical engineering practice<sup>12</sup> and approximate  $r(k_{1x})$  by a rational function of the complex variables  $k_{1x}$ . This function can be specified by its pole-zero configuration. The synthesis procedure is summarized as follows: (1) The possible modes that are needed in the waveguide are specified. These determine the guided wave poles of the transverse reflection coefficient  $r(k_{1x})$ . A rational function  $r(k_{1x})$  is constructed from the pole-zero information. (2) The G-L-M integral equation is solved to obtain the permittivity profile  $\epsilon(x)$ . The modal information is used to verify the answer.

The study of the correspondence between the poles of the transverse reflection coefficient and the modes in an inhomogeneous medium can be applied to interpret the existing results in inverse scattering. Previous results<sup>5-7</sup> are from solving the inverse problem for  $r(\omega)$  data, which is an identification problem. In Ref. 5 a two-pole, no-zero rational function is used. These examples can illustrate the analytical technique but cannot be used directly for optical waveguide design, since  $r(k_{1x})$  rather than  $r(\omega)$  should be used in the optical-waveguide-design problems. The wave equation in a dielectric medium (Fig. 1) at a certain frequency  $\omega$  is

$$\frac{\partial^2 E(k_{1x}, x)}{\partial x^2} + k_x^2 E(k_{1x}, x) = 0 \quad \text{for } x \geq 0, \quad (33)$$

which is

$$\frac{\partial^2 E(k_{1x}, x)}{\partial x^2} + k_{1x}^2 E(k_{1x}, x) = k_0^2 [\epsilon_1 - \epsilon_r(x)] E(k_{1x}, x) \quad \text{for } x \geq 0. \quad (34)$$

With  $q(x) = k_0^2 [\epsilon_1 - \epsilon_r(x)]$  the wave equation can be written in the same form as the one for  $r(\omega)$  data. The inverse-scattering theory of G-L-M<sup>5,7</sup> can then be applied directly to  $r(k_{1x})$  data.

The procedure using the inverse method to design an inhomogeneous optical waveguide can be discussed further. If the guided modes are specified in the waveguide and if the width  $d$  and the operating frequency  $\omega$  are prescribed, the problem is to determine  $\epsilon(x)$ . In general, this problem can be solved only by numerical methods. If the closed-form results obtained by applying the G-L-M theory are to be used, the first step in constructing a transverse reflection coefficient  $r(k_{1x})$  from the modal requirements is critical. This is also the main concern in this paper. So far we have discussed only part of this construction, i.e., determining the poles from the discrete modes. How to determine the zeros has not been discussed. For the homogeneous slab waveguide in Section 2, the zeros of  $r(k_{1x})$  are found from Eq. (2), which gives

$$R_{-10} + R_{01} \exp(i2k_x d) = 0. \quad (35)$$

With Eq. (3) this gives  $\exp(i2k_x d) = 1$ , so that  $k_x = n\pi/d$  for  $n = 0, \pm 1, \pm 2, \dots$ . There are an infinite number of zeros of  $r(k_{1x})$ . For a general inhomogeneous waveguide in Section 3, the zeros of  $r(k_{1x})$  are found from Eq. (17), which yields

$$\frac{B_0}{A_0} = -R_{-10} = R_{01}. \quad (36)$$

Again, this equation has an infinite number of solutions. Note that zero-condition equation (36) can be obtained by multiplying the right-hand side of pole-condition equation (18) by  $R_{01}^2$ . This implies that the zero condition and the pole condition are related.

As we saw in Section 3,  $r(k_{1x})$  in Eq. (17) is not a rational function. In other words,  $r(k_{1x})$  is not exactly a rational function with a finite number  $N$  of zeros and a finite number  $M$  of poles:

$$r(k_{1x}) = r_0 \frac{\prod_i^N (k_{1x} - k_{iz})}{\prod_i^M (k_{1x} - k_{ip})}, \quad (37)$$

where  $r_0$  is a constant,  $k_{iz}$ 's are zeros,  $k_{ip}$ 's are poles, and  $\Pi$  denotes multiplication. Since an exponential function is involved in both the numerator and the denominator,  $r(k_{1x})$  has an infinite number of poles and zeros. If a polynomial expansion (e.g., a Taylor expansion) is used in both the numerator and the denominator, the number of terms used in the expansion determines the number of zeros of the expanding function. Thus the representation with a finite number of poles and zeros of  $r(k_{1x})$  is only an approximation. It is impossible to include the infinite number of leaky poles in  $r(k_{1x})$ .

The inverse-scattering method gives a profile of  $\epsilon(x)$  extending from  $x = 0$  to  $x \rightarrow +\infty$ . Finite width  $d$  of the waveguide will require a truncation of the profile.<sup>14</sup> This is another approximation.

The following implications can be drawn from the above discussions. Rational function representations of the transverse reflection coefficient  $r(k_{1x}, \omega)$  are used to obtain closed-form solutions of the G-L-M integral equation. Since it may be difficult to extract the pole-zero configuration of the measured reflection coefficient, the rational function approach is more appropriate for the synthesis problem. In the application to optical waveguide design,  $r(k_{1x})$  data need to be prescribed for a required operating frequency and certain modal information. The possible modes in the waveguide determine the poles of  $r(k_{1x})$ . Rational function  $r(k_{1x})$  is an approximation of the true reflection coefficient, and the corresponding inverse problem can be solved in a closed form.

## 5. SUMMARY

The feasibility of applying the inverse-scattering method with a rational reflection coefficient to optical waveguide design has been studied. The pole-mode relation in the rational reflection coefficient was derived by using a stratified-medium model. It was shown that the pole condition for the transverse reflection coefficient is the same as the guidance condition for the modes in a general inhomogeneous waveguide. All the poles of the reflection coefficient correspond to the discrete modes, which are the guided and the leaky modes. The radiation modes are continuous; they do not appear as poles in the reflection coefficient but are represented by the Sommerfeld branch cut on the complex  $k_x$  plane. In the application of the rational function approach to optical waveguide synthesis, poles in the rational reflection coefficient  $r(k_{1x})$  determine the possible guided and leaky modes in the waveguide. To design the waveguide accurately requires a large

number of poles and zeros in the rational function representation of the transverse reflection coefficient.

## ACKNOWLEDGMENTS

This work was supported in part by the Joint Services Electronics Program under contract DAAL03-92-C-0001. The authors thank T. Habashy, L. S. Tamil, J. K. Shaw, and C. W. Lam for discussions.

\*Permanent address, Center for Advanced Space Sensing, Naval Research Laboratory, Washington, D.C. 20375.

## REFERENCES

1. A. K. Jordan and S. Lakshmanasamy, "Inverse scattering theory applied to the design of single-mode planar optical waveguides," *J. Opt. Soc. Am. A* **6**, 1206-1212 (1989).
2. S. Yukon and B. Bendow, "Design of waveguides with prescribed propagation constants," *J. Opt. Soc. Am.* **70**, 172-179 (1980).
3. S. R. A. Dods, "Bragg reflection waveguide," *J. Opt. Soc. Am. A* **6**, 1465-1476 (1989).
4. I. Kay, "The inverse scattering problem," Res. Rep. EM-74 (New York University, New York, 1955).
5. A. K. Jordan and H. N. Kritikos, "An application of one-dimensional inverse scattering theory for inhomogeneous regions," *IEEE Trans. Antennas Propag.* **AP-22**, 909-911 (1973).
6. D. L. Jaggard and P. V. Frangos, "The electromagnetic inverse scattering problem for layered dispersionless dielectrics," *IEEE Trans. Antennas Propag.* **AP-35**, 934-946 (1987).
7. A. K. Jordan and S. Ahn, "Inverse scattering theory and profile reconstruction," *Proc. Inst. Electr. Eng.* **126**, 945-950 (1979).
8. J. A. Kong, *Electromagnetic Wave Theory*, 2nd ed. (Wiley, New York, 1990), Chap. 3.
9. R. E. Collin, *Field Theory of Guided Waves* (McGraw-Hill, New York, 1960), Chap. 11; also see 2nd ed., 1990.
10. W. C. Chew, *Waves and Fields in Inhomogeneous Media* (Van Nostrand Reinhold, New York, 1990), Chaps. 2 and 6.
11. R. L. Liboff, *Introductory Quantum Mechanics* (Addison-Wesley, Reading, Mass., 1980), p. 205.
12. M. E. van Valkenburg, *Introduction to Modern Network Synthesis* (Wiley, New York, 1967).
13. D. Marcuse, *Light Transmission Optics* (Van Nostrand, Princeton, 1972).
14. D. W. Mills and L. S. Tamil, "A new approach to the design of graded-index guided wave devices," *IEEE Microwave Guided Wave Lett.* **1**, 87-89 (1991).